The Chilean Tornado Outbreak of May 2019:

Synoptic, mesoscale, and historical contexts

José Vicencio,[a,b] Roberto Rondanelli,[b,c] Diego Campos,[a,b] Raúl Valenzuela,[c,d] René Garreaud,[b,c] Alejandra Reyes,[a] Rodrigo Padilla,[a] Ricardo Abarca,[a] Camilo Barahona,[a] Rodrigo Delgado,[a] and Gabriela Nicora[e]

[a] *Dirección Meteorológica de Chile, Santiago, Chile*

[b] *Departamento de Geofísica, Universidad de Chile, Santiago, Chile*

[c] *Center for Climate and Resilience Research, Santiago, Chile*

[d] *Instituto de Ciencias de la Ingeniería, Universidad de O'Higgins, Rancagua, Chile*

[e] *CEILAP, UNIDEF (MINDEF-CONICET), Buenos Aires, Argentina*

Corresponding author: Roberto Rondanelli, ronda@dgf.uchile.cl

Early Online Release: This preliminary version has been accepted for publication in *Bulletin of the American Meteorological Society*, may be fully cited, and has been assigned DOI 10.1175/BAMS-D-19-0218.1. The final typeset copyedited article will replace the EOR at the above DOI when it is published.

ABSTRACT

In late May 2019, at least seven tornadoes were reported within a 24-hour period in Southern Chile (western South America, 36–38°S), including EF-1 and EF-2 events causing substantial damage to infrastructure, dozens of injuries, and one fatality. Despite anecdotal evidence and chronicles of similar historical events, the threat from tornadoes in Chile was regarded with skepticism until the 2019 outbreak.

Herein, we describe the synoptic scale features instrumental in the development of these tornadic storms, including an extended SW–NE trough along the South Pacific, with a large post-frontal instability area. Tornadic storms appear to be embedded in a modestly unstable environment (positive convective available potential energy but less than 1000 J kg^{-1}) and strong low- and mid-level wind shear, with high near-surface storm-relative helicity values (close to -200 m^2s^{-2}), clearly differing from the Great Plains tornadoes in North America (with highly unstable environments) but resembling cold season tornadoes previously observed in mid-latitudes of North America, Australia, and Europe. Reanalyzing rainfall and lightning data from the last 10 years, we found that tornadic storms in our region occur associated with locally extreme values of both CAPE and low-level wind shear, where a combination of the two in a low-level vorticity generation parameter appears as a simple first-order discriminant between tornadic and non-tornadic environments. Future research should thoroughly examine historical events worldwide to assemble a database of high-shear, low-CAPE mid-latitude storms and help improve our understanding of these storms' underlying physics.

Accepted for publication in *Bulletin of the American Meteorological Society.* DOI 10.1175/BAMS-D-19-0218.1.

CAPSULE

An unprecedented tornado outbreak occurred in Southern Chile, with at least seven tornadoes reported over a period of 24 hours, causing substantial damage, dozens of injuries, and one fatality.

Accepted for publication in *Bulletin of the American Meteorological Society.* DOI 10.1175/BAMS-D-19-0218.1.

Introduction

On 30 and 31 May 2019, two destructive tornadoes were reported in two of Southern Chile's large cities (Fig. 1). The first affected Los Ángeles (37.5°S) on 30 May, reaching an intensity of 2 on the enhanced Fujita scale (EF-2), according to the Chilean Weather Service (Vicencio et al. 2019), with estimated maximum sustained winds between 50 and 60 m s^{-1} that caused severe damage along its 5-km trajectory. On 31 May, another tornado was reported as crossing the second-largest metropolitan area in the country along a 15-km trajectory between Talcahuano and Concepción (36.8°S), with estimated winds between 50 and 55 m s-1 (EF-1 to EF-2, Aránguiz et al. 2020, see also Appendix A). During the two days, at least five other tornadoes were reported by emergency agencies, social networks, and newspapers in small towns and country areas, resulting in roof damage, displacement of vehicles, personal injuries, and one fatality (Table 1 summarizes all tornadoes and damage reports). This tornado outbreak occurred over a period of 24 hours amid severe weather conditions that also included lightning, heavy rain, and large hail (~3 cm in diameter), all of which are uncommon in South-Central Chile's generally more stable extratropical storms.

Tornadoes are considered to be among the most damaging weather events, causing millions of dollars' worth of damage and dozens of casualties annually (Brooks and Doswell 2001). The effects of tornadoes are widely known in regions where they are frequently reported, notably in the Great Plains of the central and southern United States. This area, colloquially known as "Tornado Alley," reports nearly 800 tornadoes annually (Goliger and Milford 1998)—the highest frequency on Earth—mostly during boreal spring (Brooks et al. 2003). By contrast, in South America, where some of the world's most severe storms have been identified (Zipser et al. 2006), only around 7–10 tornadoes are reported per year (Goliger and Milford 1998). An area in eastern South America—south of 20ºS, shared by Argentina, Brazil, Paraguay, and

Accepted for publication in *Bulletin of the American Meteorological Society.* DOI 10.1175/BAMS-D-19-0218.1.

Uruguay—has the highest concentration of days with favorable conditions for tornadoes, but no favorable days are shown on the western coast of South America (Brooks et al. 2003). From a sample of about 70 tornadoes registered in Brazil, no clear seasonality could be established (Silva Dias 2011).

Tornadoes in Western South America and Southern Chile are so rare that, prior to May 2019, the only reference in scientific literature appears to be a conference paper (Soliño and Schwarzkopf 1982) reporting the occurrence of five tornadoes between 1881 and 1981. Unconfirmed reports seem to be the origin of a slight shading over Central and Southern Chile appearing in a worldwide review of tornadoes, including a section about South America, mostly focused on neighboring Argentina (Goliger and Milford 1998). Because Chile lies on the southwest coast of South America, the subtropical Pacific anticyclone creates a relatively mild and stable climate, with most of its rainfall originating from cold fronts during the austral winter (Falvey and Garreaud 2007). Convection and thunderstorms are extremely infrequent in Chile compared to the rest of the continent, except in Southern Patagonia (45-50°S, Garreaud et al. 2014) and the Northern Altiplano region (Garreaud et al. 2003). Despite the relative absence of severe weather over continental Chile, reports of about 30 tornadoes and waterspouts have been collected by the Chilean Navy Weather Service since 2000 (Servicio Meteorológico de la Armada 2010). In spite of accumulated anecdotal evidence, including folklore and mythological references from pre-Columbian people (Bastias-Curivil 2019), most scientists and authorities were surprised by the tornado outbreak in late May 2019 in a country with no weather radars and no established tornado warnings. A recent independent study by Barrett et al. (2020) described the environmental and mesoscale conditions of the two main tornadoes of Los Ángeles and Talcahuano-Concepción and attributed the tornadic storms to the combination of moist warm surface air advection and cold upper tropospheric temperatures, giving rise to

Accepted for publication in *Bulletin of the American Meteorological Society.* DOI 10.1175/BAMS-D-19-0218.1.

convective available potential energy due to a mid-level trough. Substantial shear, potentially enhanced by the abrupt topography, was also postulated by Barrett et al. (2020) as a key contributor to tornadic storms.

However, the tornado outbreak prompted many questions, challenging our understanding of extreme meteorological events in Central-Southern Chile. Do Chile's environmental conditions differ from those that allow tornadoes to form in other regions of the world? What were the environmental conditions that triggered the 2019 tornado outbreak? How common are these conditions? Indeed, tornadoes in modestly buoyant environments with low convective available potential energy have been reported over continents' western coasts during wintertime (Braun and Monteverdi 1991; Blier and Batten 1994; Monteverdi and Quadros 1994; Hanstrum et al. 2002; Monteverdi et al. 2003) as well as other regions, such as the southeastern U.S. (Sherburn et al. 2016) and Europe (Clark 2009; Wesolek and Mahieu 2011). Even for high-CAPE tornadic environments, strong low-level shear (between surface and 1–3 km) appears to be a key factor compared to the presence of convective instability (Brooks 2009; Brooks et al. 2019).

The purpose of this work is to develop a synoptic and mesoscale description of the Chilean tornadoes of 30 and 31 May 2019 as we address the above-mentioned questions. We characterize the seasonality and geographical distribution of previously reported events using a tornado and waterspout database. The GOES-16 and lightning databases and reports from the ground allowed us to describe some of the mesoscale features related to the development and evolution of convective cells during this tornado outbreak. In particular, we use Aircraft Measurement Data Relay (AMDAR) data to characterize the observed thermodynamic and shear parameters during the period of the tornado outbreak. We use ERA-5 reanalysis to investigate the role of wind-shear and instability parameters in some previous tornadic storms.

Accepted for publication in *Bulletin of the American Meteorological Society.* DOI10.1175/BAMS-D-19-0218.1.

Besides our local interest in these tornadic storms, we expect to contribute to the larger global research effort to uncover the physical mechanisms and develop forecasting capabilities for these rare but potentially destructive tornadoes.

Data

Here, we briefly describe the observational data and the numerical model output used in this analysis.

- *GOES-16 RGB Air Mass.* GOES-16 satellite data (channels 8, 10, 12 and 13) were used to make RGB Air Mass composites for 2100 UTC 30 May and 1800 UTC 31 May (Lensky and Rosenfeld, 2008; EUMETSAT 2009; EUMETSAT 2015). To observe the mesoscale cloud development, 10-minute GOES-16 images from channel 13 (infrared) were used.

- *ERA5 and ECMWF Forecast.* For synoptic analysis, we used the most unstable convective available potential energy (hereafter CAPE), winds at 200, 500, 850, 1000 hPa, temperature at 500 and 850 hPa, geopotential height at 200, 500, 700, 1000 hPa, and dew point fields from ERA5 (~31 km horizontal resolution; Hersbach et al. 2020). Isentropic potential vorticity and wind at 330 K were also obtained from ERA-Interim reanalysis (Berrisford et al. 2009) at ~80 km horizontal resolution (Berrisford et al. 2009). In the case of sea level pressure (SLP) and 300 hPa winds, the data came from the ECMWF model (0.1° x 0.1°) initialized at 12 UTC each day. All data were recorded from 28–31 May 2019 every three hours.

- *Surface data and AMDAR.* To estimate precipitation intensity and accumulated amounts, we used hourly data from 50 weather rain gauges, provided by the National Water Authority (DGA) and the National Weather Service (DMC). For temperature and

Accepted for publication in *Bulletin of the American Meteorological Society.* DOI 10.1175/BAMS-D-19-0218.1.

vertical wind structure near the tornadic storms, we used Aircraft Measurement Data Relay (AMDAR; Painting 2003) measurements from flights that landed at and took off from Carriel Sur Airport (Talcahuano-Concepción) on 30 and 31 May 2019.

- *WWLLN.* The World Wide Lightning Location Network (WWLLN, http://wwlln.net) currently comprises 70 sensors across all continents detecting low frequency radio waves (sferics) emitted by lightning strokes (Virts et al. 2013; Hutchins et al. 2012). Here, we use a global database with lightning stroke localization in time and space (within ~5 km and <10 μs accuracy; Abarca et al. 2010) from January 2008 to May 2019. The global lightning detection efficiency of WWLLN ranges between 5 and 10% (Abarca et al. 2010), although recent studies estimate this global efficiency at around 15% for the year 2017 (Koronczay et al. 2019). Because it depends significantly on the discharges' maximum current, the detection efficiency can reach up to 35% for currents exceeding -130 kA (Abarca et al. 2010).

- *Weather Research and Forecasting (WRF) Simulations.* A regional numerical simulation was conducted to provide atmospheric fields at a higher temporal and spatial resolution near the tornado region. The simulation was performed using WRF 4.0.3 (Skamarock et al. 2019) and ERA-5 reanalysis fields as boundary and initial conditions. An outer domain, at 9 km resolution, was initialized at 0000 UTC 28 May 2019, while two-way nested domains configured at 3 and 1 km were initialized on 1200 UTC 30 May 2019 (Figure S1). The parameterizations used in this simulation were the Thompson microphysics scheme (Thompson et al. 2008), the Betts-Miller-Janjić cumulus parameterization (active for the outer domain only; Janjić 1994), the rapid radiative transfer model radiation parameterization (Iacono et al. 2008), the Mellor-Yamada-Nakanishi-Niino level 2.5 scheme of turbulence closure for the boundary and

Accepted for publication in *Bulletin of the American Meteorological Society.* DOI 10.1175/BAMS-D-19-0218.1.

surface layers (Nakanishi and Niino 2004, 2006), and the Noah land surface model (Niu et al. 2011).

Synoptic scale environment

An important feature of the synoptic scale environment during the tornado outbreak was the presence of a blocking anticyclone south of 45ºS (H1 in Fig. 2). This blocking anticyclone produced a split of the mid-latitude jet with a reinforced subtropical branch centered at 30ºS and extending poleward to about 35ºS (black arrows in Fig. 2; see also Figs 3, 4). The blocking anticyclone effectively reversed the climatological meridional gradient of potential vorticity (PV; Fig. 4) in the upper atmosphere over the area of 70–90ºW, which is typical of Rossby wave breaking events in this region. Cyclonic PV air is advected equatorward, while anticyclonic PV is located over the blocking high in a dipole blocking pattern (anticyclonic PV air centered at around 60º S, with cyclonic disturbances traveling at around 35ºS, Fig. 3 c–f). The reinforced equatorward branch of the split jet becomes a waveguide for short wavelength baroclinic disturbances traveling from the Southeast Pacific toward Central and Southern Chile (30–40ºS), indicated as L1, L2, L3, and L4 in the surface pressure field in Fig. 2. These lows were all embedded within a much larger-scale negatively tilted (SW-NE) trough that, at 0900 UTC 29 May, covered the region from about 100ºW to 70ºW and projected well into the lower latitudes (~ 20º S, Fig. 3). This large-scale trough is the cyclonic side of the blocking dipole, which features a large, nearly barotropic surface response with a similarly SW-NE elongated surface low, reaching South America at around 0900 UTC 29 May (Fig. 5a). Over the following three days, the large-scale low moved slowly eastward toward the continent, while the smaller-scale lows traveled along the poleward side of the subtropical jet with cloud bands rotating cyclonically around an occluded larger-scale low in a configuration that resembles a “merry-go round” pattern (Rasmussen and Turner 2003).

Accepted for publication in *Bulletin of the American Meteorological Society.* DOI 10.1175/BAMS-D-19-0218.1.

At 0900 UTC 29 May 2019, the first of these disturbances can be seen as a shortwave trough with its axis at about 87ºW at 35ºS in 500 hPa (see Fig. 3a). As the trough moves toward the continent, it rotates cyclonically, and by 2100 UTC 30 May, the axis of the trough is mostly zonal and located near 43ºS (Fig. 3d). This mid-level trough is associated with the surface low L1 (centered at about 43ºS and 80ºW) and with the large area of thunderstorms over the ocean between 35 and 40ºS (Fig. 2a). As the mid-level circulation becomes mostly zonal, pockets of cold air at the poleward side of the subtropical jet are advected toward the continent (Fig. 5, 6), replacing the relatively warm mid-tropospheric air present before 0900 UTC 30 May (Fig. 6a–b). From an upper-level dynamics perspective, these pockets of cold air may be considered cyclonic PV anomalies propagating along the poleward flank of the subtropical jet (Fig. 3) or as shortwaves in the 500 hPa geopotential height field. By 2100 UTC 30 May, the mid-level trough was already located south of the tornado region with a mostly zonal orientation (Fig. 3d). The passage of the mid-level wave destabilized the troposphere, with relatively large convective instability values, as shown by the most unstable CAPE values in the ERA-5 reanalysis—up to 400–500 J kg^{-1}with a peak at 2100 UTC 30 May, close to the time the first tornadoes were reported (Fig 6d). Instability was enhanced by low-level warm advection along the coast that peaked on 30 May, induced by the surface low L1 that remained mostly stationary from about 28 May to 31 May (Fig. 5). This warm advection is illustrated by the flow across isolines of geopotential thickness in the layer between 1000 and 700 hPa (see Figs. 6a-d). Barrett et al. (2020) discuss the possible role of topography in enhancing the northerly flow along the coast, thereby favoring both low-level warm advection and helicity, particularly during the first day of the outbreak. At the same time, the main convective instability area was located in the poleward region of a jet streak exit (Fig. 3d), where synoptic scale dynamical ascent is expected to be enhanced by secondary ageostrophic circulations (Hanstrum et al.

Accepted for publication in *Bulletin of the American Meteorological Society.* DOI 10.1175/BAMS-D-19-0218.1.

2002; Rose et al. 2004; Wesolek and Mahieu 2011; Childs et al. 2018), characteristic of cold season tornado outbreaks elsewhere (Reed and Blier 1986; Monteverdi and Quadros 1994).

On 30 May, the main low L1 became occluded with a minimum pressure of about 995 hPa (Fig. 2a) and a secondary low formed on the equatorward flank of the original low (L2 in Fig. 2a, also Fig. 5d). This surface low is connected to a second mid-level shortwave trough, whose axis is at about 85ºW on 2100 UTC 30 May (Fig. 3d). The RGB satellite image for 2100 UTC 30 May (Fig. 2a) shows a developing surface cyclone L2 with a distinct cold frontal band and a clear separation between the upper-level dry air intrusion behind the cold front (orange colors in Fig. 2a) and the relatively warmer air mass ahead of the surface front (dark green colors). Over the course of the following day, the secondary low L2 amplified and moved eastward as it interacted with the upper-level shortwave. The original cold frontal band of L2 rotated cyclonically over the course of 31 May, crossing Chile at about 43ºS (blue segmented line in Fig. 2b). Some hours before the tornadoes on 31 May, a new mesoscale cyclone (L3 in Fig 2b) developed below the cyclonic vorticity advection region of the upper-level shortwave (a convective band is visible from about 13 UTC over the ocean along 80ºW and from 34 to 38ºS) centered at about 38ºS on 1800 UTC 31 May. This new cold frontal band comprised several individual convective cells triggered over the ocean close to the continent at about 50-km intervals (see Fig 2b; two such cells can also be seen in Fig. 10b). This feature was responsible for the storms that produced two tornadoes on the afternoon of 31 May and closely fits the description of a comma cloud, which develops baroclinically at the expense of an upper-level short wave over an unstable post-frontal air mass (Rasmussen and Turner 2003; Houze, 2014). It is remarkable that a similar comma cloud feature accompanied other cold season tornado outbreaks, such as November 1982 in California (Hales 1985; Reed and Blier 1986) and December 2006 in England (Clark 2009).

Accepted for publication in *Bulletin of the American Meteorological Society.* DOI 10.1175/BAMS-D-19-0218.1.

Mesoscale analysis

Thunderstorms over the study region that accumulated up to 180 mm of rainfall between 30 and 31 May across different stations in the region (Fig. 7a) resulted in rainfall rates higher than 10 mm h^{-1} at some stations (Fig. 7b). Moreover, on 30 May, lightning activity (Fig. 7c) over the Biobío region highlights the presence of convective clouds developing at about 15 UTC until 00 UTC, moving in straight lines from northwest to southeast (320–330º, ~10 ms^{-1}), most originating inland and producing large hail (about 2–3 cm diameter; see Fig. S2). Between 1900 UTC 30 May and 0000 UTC 31 May, at least five tornadoes were reported (numbers 1 to 5 in Table 1 and Fig. 7c) along the Central Valley between 36.5ºS and 38º S (see Fig. 1). On 31 May, convective cells and lightning moved from the ocean toward the continent associated with the L3 low and comma cloud system (Fig. 2b). The Talcahuano-Concepción tornado (#6 in Table 1 and Fig. 7d) was associated with lightning activity less than 40 minutes before tornado formation and decaying shortly after. Other lightning clusters were larger in magnitude and duration, particularly those that arrived at Maule Region with one tornado reported that day in the town of Chanco (#7 in Table 1 and Fig. 7d). Perhaps due to the mesoscale instability caused by the comma cloud, some convective cells and lightning activity lasted longer than 6 h on 31 May, with a similar storm direction (320–330º) but greater magnitude (~20 m s-1) than the storms on 30 May.

Wind shear and instability

In this subsection, we track the local evolution of wind shear and instability given their crucial role in tornadic storms. Figure 8 (see also Fig. S3) shows instability and shear parameters calculated using WRF runs at the time of the two main tornadoes. During 2200 UTC 30 May 2019, the magnitude of low-level wind shear (0–1 AGL) shows modest values

Accepted for publication in *Bulletin of the American Meteorological Society.* DOI 10.1175/BAMS-D-19-0218.1.

over the ocean (between 5 and 10 m s-1) and much higher values inland (10–20 ms^{-1}). However, differences in shear between land and ocean are insubstantial over the deeper 0–6 km AGL layer, suggesting a synoptic scale or topographic origin for the deep shear. The inland low-level shear increase is partly due to weaker surface wind speeds over land (relative to offshore values) likely induced by differential friction. A more pronounced northerly component is also present at 1 km AGL that may be related to the topographic blocking of the Andes and coastal cordillera (Kalthoff et al. 2002; Barrett et al. 2009; Barrett et al. 2020; Marín et al. 2020). The near-surface northeasterly winds are almost perpendicular to the southwesterly winds at 6 km AGL (Fig. 8a and c), thus maximizing the directional wind shear. This resembles the situation during tornadic storms in California and other regions of complex topography (Monteverdi et al. 2003)

As described above, on 30 May, CAPE from reanalysis reached only moderate values of 200–400 J kg^{-1} approaching the continent from the ocean due to the prevailing mid-level westerly flow transporting cold air pockets. WRF simulations, which provide a higher resolution of the instability field, show a narrow structure of much higher CAPE along the Central Valley between 34ºS and 38ºS with values of up to 1000 J kg^{-1} at the time of the tornado in Los Ángeles (Fig. 8a). From AMDAR temperature and wind vertical profiles and WRF dew point temperature for Talcahuano-Concepción, we were able to construct skew T-log$p$ diagrams and calculate severe weather parameters from the hodographs for available flights during 30 May and 31 May using the SHARPpy toolkit (Blumberg et al. 2017, Fig. 9). The available AMDAR flight for 2052 UTC 30 May features a most unstable CAPE of 673 J kg^{-1}, consistent with values above 500 J kg^{-1} near the coast. Temperatures in the Central Valley were slightly higher than those near the coast where the profile was taken, reaching 15–16ºC in most stations prior to the initiation of convection. If the surface temperatures and humidity in

Accepted for publication in *Bulletin of the American Meteorological Society.* DOI 10.1175/BAMS-D-19-0218.1.

Talcahuano are replaced by those of the Central Valley before the thunderstorms (*T*=15ºC, *Td*=13ºC), one can easily reach surface CAPE values over 1000 J kg^{-1}. This shows that CAPE is highly sensitive to even small variations in surface temperature (an increase of about 500 J kg^{-1} per ºC), indicating even moderate surface warming during the afternoon as a possible source of these high CAPE values. This is also supported by WRF simulations that show maximum CAPE over the Central Valley simultaneously with the maximum surface temperatures. Rapid destabilization by surface warming has been identified as a key factor in the severity of low-CAPE high-shear storms in Southeastern U.S. (King et al, 2017).

A widely used measure that indicates a storm's likelihood of becoming supercellular is the storm-relative helicity (SRH) near the surface (Davies-Jones 1990; Rasmussen 2003). Figure 9 shows this quantity for 30 May near the time of the tornadoes in the Central Valley. Large values of 0–1 km SRH (calculated from the left-moving Bunkers' storm motion) range from -100 m^2s^{-2} to -250 m^2s^{-2} over the regions in which tornadoes occurred, which are within the typical tornadic storm range in continental U.S. (Rasmussen 2003; Thompson et al. 2007). AMDAR hodograph for that particular day taken at Talcahuano near the coast (Fig. 8b) confirms a relatively large value of SRH 0-1 km of about -118 m^2s^{-2}, largely explained by the 0-500 m layer. It is also remarkable that the hodograph exhibits most tornadic hodographs features (Esterheld and Giuliano 2008): a nearly straight-line shear vector in lower levels (about 9 m s^{-1}) with a kink in lower levels at about 300 m, and a surface storm relative flow vector oriented nearly orthogonal to the low-level shear, which is the ideal situation for mesocyclone development in which low-level inflow contributes mostly to streamwise vorticity.

On 31 May, WRF simulates moderate CAPE levels off the coast (~ 0 to 600 J kg^{-1}, Fig. 8 d) with smaller values over the Central Valley, except for an isolated maximum near 35ºS. Greater instability values over the ocean appear connected to the comma cloud mesoscale low

Accepted for publication in *Bulletin of the American Meteorological Society.* DOI 10.1175/BAMS-D-19-0218.1.

described in Section 3. The AMDAR profile in Talcahuano four hours before the tornado confirms relatively high unstable CAPE values of 744 J kg^{-1} and surface-based CAPE of 309 J kg^{-1} (Fig. 9). Both the surface and 1-km AGL winds increase substantially from the previous day, resulting in a longer hodograph with a maximum wind near 800 m of about 25 m s^{-1}. The corresponding AMDAR hodograph for Talcahuano at 1344 UTC (Fig. 9) shows an even higher SRH value of -229 m^2s^{-2}, again with most of the contribution coming from the layer below 500 m. In this particular case, the tornadic features of the hodograph are even more striking than those of the previous day. Besides the larger SRH values, the angle between relative inflow and low-level shear (critical angle parameter) is almost orthogonal (82º). WRF fields of 0–1 AGL SRH provide a spatial context for this individual observation. At 1800 UTC 31 May (Fig. 8d), values around -200 m^2s^{-2} are widespread with localized patches of even -600 m^2s^{-2} near the coast and along the Central Valley, roughly coinciding with the location of the observed tornadoes during this day.

Based on analysis of a large contiguous U.S. tornado database, Coffer et al. (2019) argue for the use of 0–500 m SRH as the best discriminant between tornadic and non-tornadic storms, finding that significant tornadoes appear with mean SRH magnitudes of about 220 m^2s^{-2}. For 31 May, the AMDAR profile shows an SRH between 0-500 m of about -160 m^2s^{-2}; however, if one replaces the calculated storm motion with the actual storm motion observed from GOES-IR, SRH 0-500 m rises to about -200 m^2s^{-2}, a magnitude well above the no-tornado interquartile range and more typical of the weak and significant tornado categories in Coffer et al.'s (2019) analysis. By inspecting the WRF simulations, we see that the highest SRH values are associated with the propagation of the comma cloud structure eastward toward the continent, which is far less organized in WRF than in GOES infrared imagery. However, one can speculate that near-surface baroclinicity present at the surface front of the comma cloud structure could enhance

Accepted for publication in *Bulletin of the American Meteorological Society.* DOI 10.1175/BAMS-D-19-0218.1.

the low-level shear by thermal wind balance and thereby favor tornadogenesis on 31 May. The absence of a similarly organized mesoscale structure on 30 May may explain that day's relatively weaker SRH values (Fig. 8b, d).

Storm evolution from GOES-IR

The storm that originated the tornado in Los Ángeles (30 May) was one of five that formed during the evening of 30 May over the moderate CAPE region within the Central Valley. GOES infrared images show the initiation of the storm at about 2127 UTC (thin black contour in Fig. 10a) about 20 km northwest of the tornado. As the storm moved southeasterly, severe weather was reported near Los Ángeles, including large hail (> 2 cm diameter; Fig. S2a), heavy rain, and lightning starting about 20 min before tornadogenesis (see Fig. 2c). Around 2157 UTC, a tornado is observed in northeastern Los Ángeles, located in the rear (upshear) poleward quadrant relative to the storm's center following a mostly north–south trajectory (dashed line in Fig. 10a). The tornadic storm develops a secondary region of ascent ten minutes later (2207 UTC) in the same quadrant in which the tornado was located (in Fig. 10a, cloud tops lower than -46 C are plotted in gray lines). The convective cell lasted around 3 hours in total from first sight in the IR images at 2000 UTC until no updraft could be identified at 2300 UTC. Given the top brightness temperature as an indication, the depth of the convective storm was around 9 km. Following the motion of the updraft in the GOES images, a storm motion vector of 328º and 12 m s^{-1} may be derived.

Figure 10b tracks the evolution of the storm that affected Talcahuano-Concepción on 31 May. Between 1700 and 1800 UTC, the storm increased, with around 20 lightning flashes identified by WWLLN before 1730 (Fig. 7d). Once the convective system was inland, the tornado had already commenced its path over the city at 1800 UTC. Again, the tornado is located in the rear poleward (rear-right) quadrant of the storm relative to the motion of the

Accepted for publication in *Bulletin of the American Meteorological Society.* DOI 10.1175/BAMS-D-19-0218.1.

coldest cloud top. The observed trajectory of the tornado closely follows the trajectory of the coldest cloud top separated by about 15 km, indicating the tornado's position relative to the center of the updraft.

In the absence of radar data, some observational indications that tornadoes were embedded within supercellular storms can be gained from the GOES-16 satellite images (Fig. 10, Table 1): most storms have minimum brightness temperatures near 215 K (corresponding to a height between 12 and 15 km according to soundings 500 km south and north of Concepción), an indication that overshooting tops reached the tropopause on 31 May, sometimes developing characteristic enhanced-V, cold-U signatures and nearby warm areas in the anvil (Fujita 1982; Adler et al. 1981; Moller et al. 1994; Brunner et al. 2007; Peyraud 2013). Some storms showed a flanking line, characteristic of classic supercells (Moller et al. 1994). In all seven tornadoes, the overshooting tops in the infrared images are located close to the tornadoes at the surface (Lemon and Doswell 1979; Markowski and Richardson 2011) in the rear flank of the cell (relative to the storm's motion). The tornadoes of Talcahuano-Concepción and Los Ángeles (see. Fig. 10) are located about 10 km away from the updraft, in the region of brightness temperature warmer than -35ºC and along the storm motion's direction. As suggested by B. Barrett (personal communication), this may be interpreted as a strongly sheared updraft and a further indication of these storms' supercellular nature.

Common to other tornadic storms described in the literature, the time evolution of the overshooting top in the infrared indicates a rapid cooling between 50 to 10 minutes before the appearance of a tornado at the surface followed by a relative warming of the updraft region at the time of tornadogenesis (see Peyraud 2013 and references therein). The IR features found in each of the storms are summarized in Table 1.

Accepted for publication in *Bulletin of the American Meteorological Society.* DOI 10.1175/BAMS-D-19-0218.1.

Additional evidence for supercellular tornadogenesis comes from videos and pictures of the two main tornadoes that show the existence of a cloud wall surrounding the tornadoes while clear slots attest the parent mesocyclone and rear downdraft (Fig. S2b). The duration of the cells (2–3 hours) and the size derived from the infrared are also characteristic of supercells. Higher resolution numerical simulations and analysis of the propagation of the Los Ángeles and Concepción cells performed by Barrett et al. (2020), in addition to our own, give further credence to the supercell nature of the tornadic storms. Storm motion of the left-moving supercell calculated using the SHARPpy toolkit (Bunkers et al. 2014; Blumberg et al. 2017) confirms the storm motion derived for each tornado based on GOES-IR observations (Table 1).

Severe storm environment for tornadoes in Chile

Seasonal and geographical distribution of historical tornadoes

From 1633 to 2019, at least 43 tornadoes were reported in Central and Southern Chile, comprising a database created and constantly updated by the Chilean Navy Weather Service (Servicio Meteorológico de la Armada 2010) and DMC in recent years (Fig. 1). As described by Alonso de Ovalle in one of the first chronicles of colonial life in Chile (de Ovalle 1703), on 14 May 1633, the Spanish fortress town of Carelmapu was almost completely destroyed by a tornado (see circle around 42ºS in Fig. 1). The description is so vivid that it even contains information about the size of hail 'without exaggeration … thicker than larger musket balls', which translates to about 2–4 cm diameter, or a sedimentation velocity of about 20 to 30 m s^{-1}. Hail of similar size was reported on social networks during the May 2019 storms near the Los Ángeles tornado (Fig. S2a). A better-known historical tornado crossed Concepción on 27 May 1934, causing considerable damage along a northwest–southeast trajectory. This storm

Accepted for publication in *Bulletin of the American Meteorological Society*. DOI 10.1175/BAMS-D-19-0218.1.

was covered by the *New York Times*, indicating damage worth 1 million dollars at the time (*New York Times*, 1934). From 2000 to the present, reports of about 40 different tornadoes and waterspouts (86% of total observations) can be found in the press and social media. As Figure 1 illustrates, tornado reports have increased toward Southern Chile, reaching a maximum density near 37°S (Ñuble and Biobío regions) and around 41°S (Los Lagos region). Sixty-nine percent of all recorded tornadoes occurred between 2015 and 2019. Increased social network use and high cell phone coverage, even in rural areas, may explain the apparent recent prevalence of tornadoes in Chile. Alternatively, the increase in tornado reports could be a real climate signal associated either with recent natural decadal variability or anthropogenic climate change, which are known to be at play in recent drying trends over the same region (Boisier et al. 2016) .

Another important feature is that the maximum frequency occurs during fall and winter, denoted by pale blue and blue dots in Figure 1. The peak frequency occurs during fall with 17 tornadoes reported (46%) followed by winter season with 16 tornadoes (43%). Most tornadoes occurred during the month of May, including those from Carelmapu and Concepción in 1633 and 1934 and the 2019 outbreak, mirroring the seasonality found in southwest Australia, California and England, where the maximum frequency occurs during the cool season (Blier and Batten 1994; Hanstrum et al. 2002; Kirk 2014).

CAPE and shear

This subsection aims to contextualize the late-May 2019 tornadic storms more broadly and to examine how exceptional the dynamical and thermodynamic conditions concurrent with their development were. We begin by considering the large-scale environment that form rainstorms in South-Central Chile using reanalysis to characterize the shear and instability environments of severe storms, as earlier studies have (e.g. Brooks 2009; Taszarek et al. 2018).

Accepted for publication in *Bulletin of the American Meteorological Society*. DOI 10.1175/BAMS-D-19-0218.1.

These synoptic conditions are synthesized in Fig 11. Relative to dry days (black dots), those days with more than 1 mm of rainfall (gray circles) exhibit higher most unstable CAPE (10–50 J kg^{-1}) and higher bulk shear values (5–10 m s^{-1}) in connection with stronger-than-average winds aloft. CAPE and shear exhibit some positive correlation, and the precipitation amount (reflected in the symbol size) tends to increase with both low-level wind shear and CAPE. Let us now examine the synoptic conditions during lightning storms as an indicator of unstable conditions. Given the formation mechanism of electrical strokes in the atmosphere, lightning activity tends to increase with convective rainfall and other storm metrics (Pessi and Businger 2009). Over the central U.S., strokes almost double in frequency in tornadic storms relative to non-tornadic storms (Turman and Tettelbach 1980). Consistent with the mostly stable nature of the cold frontal systems, lightning occurrence along the Chilean coast is notoriously low except for a well-defined maximum in western Patagonia (south of 42°S; Garreaud et al. 2014). For the present study, we consider a 3° x 3° box centered at [37ºS, 72.5ºW], thus encompassing the cities of Concepción and Los Ángeles in the Biobío region. Only 47 days in the 11-year record have more than 25 WWLLN strokes (Section 2), including 30 and 31 May 2019 (with 84 and 239 strokes, respectively). The corresponding CAPE-Shear values for 30–31 May 2019 are highlighted (orange and red circles) in Fig. 11a. CAPE values are similar on both days (100-200 J kg^{-1}; notice that these are daily means of ERA-5 reanalysis) and within the upper tail of the distribution. Likewise, the wind shear values are also similar (about 15 m s^{-1}) and well above the interquartile range of lightning storms. The CAPE-wind shear values of the other three tornadic storms in this region are also in the upper parts of their respective distributions (Fig. 11a). From this simple analysis, we infer that substantial CAPE values are a necessary condition for the occurrence of tornadic storms in South-Central Chile; however, these values do not differ significantly from those of lightning storms. If we consider the five tornadic storm

Accepted for publication in *Bulletin of the American Meteorological Society.* DOI 10.1175/BAMS-D-19-0218.1.

days shown in Fig. 11a, this subset exhibits low-level wind shear values (higher than about 12 m s^{-1}), well above the typical range of rainy or even thunderstorm days for the region.

Low-level vorticity generation parameter (VGP)

Motivated by the fact that the generation of vertical vorticity by tilting of horizontal vorticity is proportional to the updraft speed times the magnitude of the vertical shear (e.g., Rasmussen and Blanchard 1998; Markowski and Richardson 2011), authors have attempted different combinations of shear and CAPE to discriminate between severe and non-severe thunderstorm environments. For instance, Brooks (2009) shows probabilities of severe thunderstorms as a function of mixed-layer CAPE and 0–6 km wind shear, concluding that even the simple product of the two can be a valuable forecasting parameter.

Rasmussen and Blanchard (1998) noted that, within parcel theory, the maximum velocity of an updraft is proportional to $\sqrt{CAPE}$, and given that vertical shear of the horizontal wind is the main contributor to horizontal vorticity, they defined VGP (ms^{-2}) as the product of $\sqrt{CAPE}$ and the mean shear between 0 and 4 km. VGP has appeared in the recent literature under other terminology and with different physical units: for instance, Tsonevsky et al. (2018) calculate shear between 925 and 500 hPa pressure level and call the product with CAPE "CAPE-SHEAR" or "CAPES", suggesting that it is a better predictor of severe weather in high-shear, low-CAPE environments. VGP may be considered a simple way to consider instability and wind shear to evaluate the possibility that an environment will generate vertical vorticity by tilting, which is regarded as the physical process responsible for the formation of a mid-level mesocyclone within a supercell thunderstorm (Markowski and Richardson 2011). Although the formation of a supercell is known to be favored by the deep-layer shear (typically 0–6 km), low-level shear (between the surface and 1 km AGL) seems to be instrumental for the

Accepted for publication in *Bulletin of the American Meteorological Society*. DOI 10.1175/BAMS-D-19-0218.1.

mesocyclone's ability to produce strong low-level vertical accelerations and provide the correct alignment between the mesocyclone and surface-vertical vorticity (Coffer and Parker 2017; Guarriello et al. 2018; Sherburn and Parker 2019), which favors tornadogenesis. This has led authors to propose even shallower layers for the calculation of severe weather parameters, such as the SRH (Coffer et al. 2019) to distinguish ordinary from tornadic supercells. Following these arguments, we calculate here a low-level VGP as a discriminant between tornadic and non-tornadic storms in our region. Figure 11a shows two isolines of the product of $\sqrt{CAPE}$ and 0-1 AGL shear from reanalysis ($VGP_{0\text{-}1}$). The five tornado days found in the study region and period show values of $VGP_{0\text{-}1}$ greater than 0.1 ms^{-2}, and the stronger tornado of Los Ángeles is within the 0.2 ms^{-2} isoline (partly helped by one of the highest CAPE values within the entire period considered). For the limited number of cases available, these thresholds appear to be a useful first-order discriminant. Thresholds are of course highly dependent on the time and space resolution of the analysis used to construct them, as attested by the much higher most unstable CAPE values in our WRF simulations compared to the ERA-5 reanalysis. As in other cold season cases, deep-layer shear offers little discriminating power since deep shear is usually available during winter at this extratropical latitude. This can be seen in CAPE-Shear scatter plots for deeper levels (Fig. 11b–c) where more storms (and even dry cases) can have shear values comparable to those in tornadic situations. Given the proximity to the coast and available humidity, other parameters deemed important in the U.S., such as the lifting condensation level, also appear less critical for this region.

Summary

In this final section, we summarize the main synoptic, mesoscale and historical aspects of tornadoes in Chile, considering the late-May 2019 outbreak. At least seven tornadoes were

Accepted for publication in *Bulletin of the American Meteorological Society.* DOI 10.1175/BAMS-D-19-0218.1.

reported between 30 and 31 May 2019, in a historical tornado hotspot in the area (around 37ºS), matching the peak frequency observed in previous reported tornadoes during late fall.

Tornadic storms were promoted by the presence of a blocking anticyclone off austral Chile and a quasi-stationary low farther north, and a cold air advection around 35–37ºS at mid and high levels of the troposphere. The location of the quasi-stationary low near the surface was such that warm air advection along the coast between 35ºS and 40ºS enhanced instability over a period of about four days. The interaction between the unstable air above the low and the passage of mid-level shortwaves traveling along the enhanced subtropical jet, initiated convection over the Central Valley of Southern Chile on 30 May 2019 and on a more organized quasilinear band of convection associated with a comma cloud on 31 May 2019 (see schematic in Fig. 12).

Based on mesoscale simulations conducted with WRF, instability peaked several hours before the tornado reports with most unstable CAPE values ranging between 500 and 1000 J kg^{-1}. AMDAR profiles taken at Talcahuano-Concepción airport agree with these values of instability, showing that about half of the CAPE is contained in the lower 4 km of the sounding. Relatively large values of SRH related to high low-level shear values were present during the two-day outbreak, based on WRF simulations and AMDAR profiles. Severe weather, including large hail and lightning activity, was present between 20 and 40 minutes before each tornado sighting. Inspection of GOES-16 infrared images (GOES-IR) reveals several characteristics observed in supercellular tornadic storms: the development of a single overshooting that suffers a relative warming 20 to 10 minutes before tornadogenesis; enhanced-V cold-U signatures; flanking lines; and an apparent sheared updraft, by contrasting the surface tornado’s position with that of the corresponding updraft. The storm motion derived from GOES-IR for the seven

Accepted for publication in *Bulletin of the American Meteorological Society.* DOI 10.1175/BAMS-D-19-0218.1.

tornadoes closely follows the storm motion derived from the AMDAR profiles for the left-mover storm, as would be expected from supercells in the Southern Hemisphere.

Although CAPE values are relatively low compared to those found in the world's main areas of severe convection (U.S. Great Plains, Argentina), they are extraordinary for Southern Chile climatology. On the other hand, low-level shear values are comparable to the ones in most tornadic regions of the world. Revisiting earlier literature on cold season tornadoes in Australia and California (Monteverdi et al. 2003) and on the basis of our own analysis and that of Barrett et al. (2020), we found that Chilean tornadoes conform to the major synoptic scale ingredients described as environmental factors that favor the occurrence of tornadoes during the cold season on other continents: strong low-level wind shear, moderate values of instability, the presence of a diffluent through in mid-levels equatorward of a mid-latitude cyclone and close to the coast, among others (Hanstrum et al. 2002). Recent discussion in the literature points to the critical role of low-level shear both in the generation of the mesocyclone (and therefore the supercell) and in the generation of tornadogenesis once the mesocyclone is established. Even for our limited sample of cases, the May 2019 tornado outbreak seems to support this view: observations taken before the Talcahuano tornado show particularly large low-level shear values and, more specifically, large SRH values concentrated in a shallow layer near the surface. Despite the large shear and SRH values, indices such as the significant tornado parameter (e.g. Blumberg et al. 2017) would not have produced tornado alarms for our case, perhaps by giving too much weight to CAPE values compared to shear and SRH. Given the low frequency of these events, refining the parameters for predicting environments favorable for tornado occurrence under low-CAPE high-shear conditions may require the synthesis of worldwide available observations under low-CAPE high-shear environments in a single

Accepted for publication in *Bulletin of the American Meteorological Society.* DOI 10.1175/BAMS-D-19-0218.1.

dataset. In the meantime, low-level VGP emerges as a useful metric to synthetize relevant ingredients (shear and CAPE) for tornado occurrence from our limited sample of cases. In the absence of nearby radiosonde stations and radar, we show that AMDAR profiles provide useful and critical information that may be used in real time for severe weather warnings.

ACKNOWLEDGMENTS

C.B. and R. A. acknowledge the Chilean National Weather Service for funding a field reconnaissance visit to obtain information about the destruction caused by the Talcahuano-Concepción and Los Ángeles tornadoes and for the WRF simulations used in this research. We appreciate the contribution of the National Emergency Office from Ñuble region for confirming the information on the tornadoes in Yungay, San Carlos, and Coihueco. GOES data were provided by NOAA via Amazon Web Services. . R.R, R.V and R.G acknowledge funding from FONDAP-ANID 151110009. RR also acknowledges funding from FONDECYT-ANID 1181781. We appreciate comments and suggestions by Brad Barrett and two anonymous reviewers that helped to improve the content and presentation of the manuscript.

Appendix A

Tornado path and surface data

The tornado that affected Los Ángeles on 30 May was first observed at 2157 UTC over the northeastern part of the city (Fig. 8a) moving southward from a rural sector and entering the urban area around 2200 UTC. Damage occurred along a 5-km path over less than ten minutes, completely destroying one factory, damaging dozens of houses' roofs, felling trees, overturning trucks, displacing cars and trucks by several meters, and injuring dozens (Table 1; Vicencio et al. 2019). Over six thousand people were affected by power outages. The intensity of this

Accepted for publication in *Bulletin of the American Meteorological Society.* DOI 10.1175/BAMS-D-19-0218.1.

tornado was estimated on the enhanced Fujita scale as 2 (EF-2), with maximum winds reaching 50–60 m s^{-1}.

On 31 May, a second tornado crossed the country's second-largest city, known as Gran Concepción. The tornado was first observed by a commercial airplane pilot as a waterspout over the sea near the coast (Claudia Ponce, personal communication), making landfall shortly after report at Caleta El Soldado around 1750 UTC (first black dot in Fig. A1b). The tornado's inland trajectory was about 15 km between Talcahuano and Concepción, with a total duration of 15 minutes (Fig. A1b). Most damage was observed over Talcahuano city (in the first half of the trajectory), including 50,000 people affected by power outages, roof damage to dozens of houses and factories, cars displaced by several meters, and one fatality, leading to intensity estimates ranging from EF-1 to EF-2 (Vicencio et al. 2019; Aránguiz et al. 2020).

The odds of a weather station sampling a tornado are very low (only a few dozen such cases have been reported for the U.S. in over 100 years (Karstens et al. 2010; Edwards et al. 2013)); remarkably, the 31 May tornado over Talcahuano was measured at Carriel Sur Airport. Its northwest–southeast trajectory was located around 400 m from two automatic weather stations close to the airport runway (AVIMET and MIDAS in Fig. A2a). After 1800 UTC, both weather stations recorded an abrupt pressure drop, descending 2.1 hPa in 6 minutes at AVIMET and 1.9 hPa at MIDAS. The minimum pressure was observed simultaneously at 1806 UTC together with an initial decrease and subsequent increase in wind speed, reaching a maximum of 24.4 m s^{-1} at 18:05 on AVIMET and 23.8 m s^{-1} at 1806 UTC on MIDAS (bottom panels in Fig. A2). A picture taken from the runway of Carriel Sur Airport (Fig. A2b) shows the tornado touching

Accepted for publication in *Bulletin of the American Meteorological Society*. DOI 10.1175/BAMS-D-19-0218.1.

the surface and moving toward the southeast several minutes before being measured by AVIMET and MIDAS weather stations.

Assuming that the maximum tangential velocity is located around 80 m from the center of the tornado (damage from the ground was estimated to occur over a maximum extension of about 150 m wide), this velocity may be estimated using theoretical profiles from the literature (Wood and White 2011). Parameters from Kato et al. (2015) give an estimate of 50–55 m s^{-1} for the maximum surface wind strength (upper EF1 or lower EF2 in the enhanced Fujita scale), consistent with the upper limit of intensity inferred from damage assessed in the field by the Chilean Weather Service (Vicencio et al., 2019) and with damage assessment developed by Aránguiz et al. (2020).

REFERENCES

Abarca, Sergio F., Kristen L. Corbosiero, and Thomas J. Galarneau Jr. 2010. “An Evaluation of the Worldwide Lightning Location Network (WWLLN) Using the National Lightning

Accepted for publication in *Bulletin of the American Meteorological Society*. DOI 10.1175/BAMS-D-19-0218.1.

Detection Network (NLDN) as Ground Truth.” *Journal of Geophysical Research* 115 (D18): L05807.

Adler, Robert F., Douglas D. Fenn, and Douglas A. Moore. 1981. “Spiral Feature Observed at Top of Rotating Thunderstorm.” *Monthly Weather Review* 109 (5): 1124–29.

Aránguiz, Rafael, Boris Saez, Gladys Gutiérrez, Claudio Oyarzo-Vera, Eduardo Nuñez, Catalina Quiñones, Romina Bobadilla, and María Teresa Bull. 2020. “Damage Assessment of the May 31st, 2019, Talcahuano Tornado, Chile.” *International Journal of Disaster Risk Reduction* 50 (November): 101853.

Barrett, Bradford S., Renéd Garreaud, and Mark Falvey. 2009. “Effect of the Andes Cordillera on Precipitation from a Midlatitude Cold Front.” *Monthly Weather Review* 137 (9): 3092–3109.

Barrett, Bradford S., Julio C. Marin, and Martin Jacques-Coper. 2020. “A Multiscale Analysis of the Tornadoes of 30–31 May 2019 in South-Central Chile.” *Atmospheric Research* 236 (May): 104811.

Bastias-Curivil, C. 2019. “Influencias de Los Procesos Geológicos En La Cosmovisión Mapuche, Entre Concepción Y Chiloé,.” Geologist, Universidad de Chile.

Berrisford, Paul, D. Dee, K. Fielding, M. Fuentes, P. Kallberg, S. Kobayashi, and S. Uppala. 2009. “The ERA-Interim Archive.” *ERA Report Series*, ERA Report Series, , no. 1 (August): 16.

Blier, Warren, and Karen A. Batten. 1994. “On the Incidence of Tornadoes in California.” *Weather and Forecasting* 9 (3): 301–15.

Blumberg, William G., Kelton T. Halbert, Timothy A. Supinie, Patrick T. Marsh, Richard L. Thompson, and John A. Hart. 2017. “SHARPpy: An Open-Source Sounding Analysis Toolkit for the Atmospheric Sciences.” *Bulletin of the American Meteorological Society* 98 (8): 1625–36.

Accepted for publication in *Bulletin of the American Meteorological Society*. DOI 10.1175/BAMS-D-19-0218.1.

Boisier, Juan P., Roberto Rondanelli, René D. Garreaud, and Francisca Muñoz. 2016. "Anthropogenic and Natural Contributions to the Southeast Pacific Precipitation Decline and Recent Megadrought in Central Chile." *Geophysical Research Letters* 43 (1): 413–21.

Braun, Scott A., and John P. Monteverdi. 1991. "An Analysis of a Mesocyclone–Induced Tornado Occurrence in Northern California." *Weather and Forecasting* 6 (1): 13–31.

Brooks, Harold E. 2009. "Proximity Soundings for Severe Convection for Europe and the United States from Reanalysis Data." *Atmospheric Research* 93 (1): 546–53.

Brooks, Harold E., and C. A. Doswell. 2001. "Normalized Damage from Major Tornadoes in the United States." *Weather and Forecasting* 16: 168–76.

Brooks, Harold E., Charles A. Doswell III, Xiaoling Zhang, A. M. Alexander Chernokulsky, Eigo Tochimoto, Barry Hanstrum, Ernani de Lima Nascimento, David M. L. Sills, Bogdan Antonescu, and Brad Barrett. 2019. "A Century of Progress in Severe Convective Storm Research and Forecasting." *Meteorological Monographs* 59: 18.1–18.41.

Brooks, Harold E., James W. Lee, and Jeffrey P. Craven. 2003. "The Spatial Distribution of Severe Thunderstorm and Tornado Environments from Global Reanalysis Data." *Atmospheric Research* 67-68 (July): 73–94.

Brunner, Jason C., Steven A. Ackerman, A. Scott Bachmeier, and Robert M. Rabin. 2007. "A Quantitative Analysis of the Enhanced-V Feature in Relation to Severe Weather." *Weather and Forecasting* 22 (4): 853–72.

Bunkers, Matthew J., David A. Barber, Richard L. Thompson, Roger Edwards, and Jonathan Garner. 2014. "Choosing a Universal Mean Wind for Supercell Motion Prediction." *Journal of Operational Meteorology* 2 (11). https://www.researchgate.net/profile/Roger_Edwards3/publication/270544768_Choosin

Accepted for publication in *Bulletin of the American Meteorological Society.* DOI 10.1175/BAMS-D-19-0218.1.

g_a_universal_mean_wind_for_supercell_motion_prediction/links/54b6f5d70cf2e68eb2800503.pdf.

Childs, Samuel J., Russ S. Schumacher, and John T. Allen. 2018. “Cold-Season Tornadoes: Climatological and Meteorological Insights.” *Weather and Forecasting* 33 (3): 671–91.

Clark, Matthew R. 2009. “The Southern England Tornadoes of 30 December 2006: Case Study of a Tornadic Storm in a Low CAPE, High Shear Environment.” *Atmospheric Research* 93 (1): 50–65.

Coffer, Brice E., and Matthew D. Parker. 2017. “Simulated Supercells in Nontornadic and Tornadic VORTEX2 Environments.” *Monthly Weather Review* 145 (1): 149–80.

Coffer, Brice E., Matthew D. Parker, Richard L. Thompson, Bryan T. Smith, and Ryan E. Jewell. 2019. “Using Near-Ground Storm Relative Helicity in Supercell Tornado Forecasting.” *Weather and Forecasting* 34 (5): 1417–35.

Davies-Jones, R. P. 1990. “Test of Helicity as a Forecast Parameter.” In *Preprints, 16th Conf. on Severe Local Storms, Kananaskis Park, AB, Canada, 1990*. Amer. Meteor. Soc. https://ci.nii.ac.jp/naid/10021166787/.

Esterheld, John M., and Donald J. Giuliano. 2008. “Discriminating between Tornadic and Non-Tornadic Supercells: A New Hodograph Technique.” *E-Journal of Severe Storms Meteorology* 3 (2). http://ejssm.org/ojs/index.php/ejssm/article/viewArticle/33.

EUMETSAT, 2009: Best practices for RGB compositing of multi-spectral imagery. User Services Division, 8 pp. [Available online at http://oiswww.eumetsat.int/~idds/html/doc/best_practices.pdf.]

EUMETSAT, 2015: Airmass RGB. 17 pp. [Available online at oiswww.eumetsat.int/~idds/html/doc/airmass_interpretation.pdf.]

Falvey, Mark, and René Garreaud. 2007. “Wintertime Precipitation Episodes in Central Chile: Associated Meteorological Conditions and Orographic Influences.” *Journal of*

Accepted for publication in *Bulletin of the American Meteorological Society*. DOI 10.1175/BAMS-D-19-0218.1.

Hydrometeorology 8 (2): 171–93.

Fujita, T. Theodore. 1982. “Principle of Stereoscopic Height Computations and Their Applications to Stratospheric Cirrus over Severe Thunderstorms.” *Journal of the Meteorological Society of Japan. Ser. II* 60 (1): 355–68.

Garreaud, René D., M. Gabriela Nicora, Rodrigo E. Bürgesser, and Eldo E. Ávila. 2014. “Lightning in Western Patagonia.” *Journal of Geophysical Research, D: Atmospheres* 119 (8): 4471–85.

Garreaud, René D., Mathias Vuille, and Amy C. Clement. 2003. “The Climate of the Altiplano: Observed Current Conditions and Mechanisms of Past Changes.” *Palaeogeography, Palaeoclimatology, Palaeoecology* 194 (1): 5–22.

Goliger, A. M., and R. V. Milford. 1998. “A Review of Worldwide Occurrence of Tornadoes.” *Journal of Wind Engineering and Industrial Aerodynamics* 74-76 (April): 111–21.

Guarriello, Felicia, Christopher J. Nowotarski, and Craig C. Epifanio. 2018. “Effects of the Low-Level Wind Profile on Outflow Position and Near-Surface Vertical Vorticity in Simulated Supercell Thunderstorms.” *Journal of the Atmospheric Sciences* 75 (3): 731–53.

Hales, John E. 1985. “Synoptic Features Associated with Los Angeles Tornado Occurrences.” *Bulletin of the American Meteorological Society* 66 (6): 657–62.

Hanstrum, Barry N., Graham A. Mills, Andrew Watson, John P. Monteverdi, and Charles A. Doswell III. 2002. “The Cool-Season Tornadoes of California and Southern Australia.” *Weather and Forecasting* 17 (4): 705–22.

Hersbach, Hans, Bill Bell, Paul Berrisford, Shoji Hirahara, András Horányi, Joaquín Muñoz- Sabater, Julien Nicolas, et al. 2020. “The ERA5 Global Reanalysis.” *Quarterly Journal of the Royal Meteorological Society* 146 (730): 1999–2049.

Accepted for publication in *Bulletin of the American Meteorological Society*. DOI 10.1175/BAMS-D-19-0218.1.

Houze, Robert A. Jr. 2014. *Cloud Dynamics*. Academic Press.

Hutchins, M. L., R. H. Holzworth, J. B. Brundell, and C. J. Rodger. 2012. “Relative Detection Efficiency of the World Wide Lightning Location Network.” *Radio Science* 47 (6). https://agupubs.onlinelibrary.wiley.com/doi/abs/10.1029/2012RS005049.

Iacono, Michael J., Jennifer S. Delamere, Eli J. Mlawer, Mark W. Shephard, Shepard A. Clough, and William D. Collins. 2008. “Radiative Forcing by Long-Lived Greenhouse Gases: Calculations with the AER Radiative Transfer Models.” *Journal of Geophysical Research, D: Atmospheres* 113 (D13). https://agupubs.onlinelibrary.wiley.com/doi/abs/10.1029/2008jd009944.

Janjić, Zaviša I. 1994. “The Step-Mountain Eta Coordinate Model: Further Developments of the Convection, Viscous Sublayer, and Turbulence Closure Schemes.” *Monthly Weather Review* 122 (5): 927–45.

Kalthoff, Norbert, Inge Bischoff-Gauß, Melitta Fiebig-Wittmaack, Franz Fiedler, Jutta Thürauf, Enrique Novoa, Clotilde Pizarro, et al. 2002. “Mesoscale Wind Regimes in Chile at 30 S.” *Journal of Applied Meteorology* 41 (9): 953–70.

King, J. R., M. D. Parker, K. D. Sherburn, and G. M. Lackmann, 2017: Rapid Evolution of Cool Season, Low-CAPE Severe Thunderstorm Environments. *Wea. Forecasting*, **32**, 763–779, https://doi.org/10.1175/WAF-D-16-0141.1.

Kirk, Peter J. 2014. “An Updated Tornado Climatology for the UK: 1981--2010.” *Weather* 69 (7): 171–75.

Koronczay, Dávid, János Lichtenberger, Mark A. Clilverd, Craig J. Rodger, Stefan I. Lotz, Dmitry V. Sannikov, Nina V. Cherneva, et al. 2019. “The Source Regions of Whistlers.” *Journal of Geophysical Research, [Space Physics]* 124 (7): 5082–96.

Accepted for publication in *Bulletin of the American Meteorological Society*. DOI 10.1175/BAMS-D-19-0218.1.

Lemon, Leslie R., and Charles A. Doswell. 1979. “Severe Thunderstorm Evolution and Mesocyclone Structure as Related to Tornadogenesis.” *Monthly Weather Review* 107 (9): 1184–97.

Lensky, I. M., and D.Rosenfeld, 2008: Clouds–Aerosols–Precipitation Satellite Analysis Tool (CAPSAT). *Atmos. Chem. Phys.*, **8**, 6739–6753, doi:10.5194/acp-8-6739-2008.

Marín, Julio C., Bradford S. Barrett, and Diana Pozo. 2020. “The Tornadoes of 30–31 May 2019 in South-Central Chile: Sensitivity to Topography and SST.” *Atmospheric Research*, October, 105301.

Markowski, Paul, and Yvette Richardson. 2011. *Mesoscale Meteorology in Midlatitudes*. John Wiley & Sons.

Moller, Alan R., Charles A. Doswell, Michael P. Foster, and Gary R. Woodall. 1994. “The Operational Recognition of Supercell Thunderstorm Environments and Storm Structures.” *Weather and Forecasting* 9 (3): 327–47.

Monteverdi, John P., Charles A. Doswell, and Gary S. Lipari. 2003. “Shear Parameter Thresholds for Forecasting Tornadic Thunderstorms in Northern and Central California.” *Weather and Forecasting* 18 (2): 357–70.

Monteverdi, John P., and John Quadros. 1994. “Convective and Rotational Parameters Associated with Three Tornado Episodes in Northern and Central California.” *Weather and Forecasting* 9 (3): 285–300.

Nakanishi, Mikio, and Hiroshi Niino. 2004. “An Improved Mellor--Yamada Level-3 Model with Condensation Physics: Its Design and Verification.” *Boundary-Layer Meteorology* 112 (1): 1–31.

———. 2006. “An Improved Mellor--Yamada Level-3 Model: Its Numerical Stability and Application to a Regional Prediction of Advection Fog.” *Boundary-Layer Meteorology* 119 (2): 397–407.

Accepted for publication in *Bulletin of the American Meteorological Society*. DOI 10.1175/BAMS-D-19-0218.1.

Niu, Guo-Yue, Zong-Liang Yang, Kenneth E. Mitchell, Fei Chen, Michael B. Ek, Michael Barlage, Anil Kumar, et al. 2011. “The Community Noah Land Surface Model with Multiparameterization Options (Noah-MP): 1. Model Description and Evaluation with Local-Scale Measurements.” *Journal of Geophysical Research, D: Atmospheres* 116 (D12). https://agupubs.onlinelibrary.wiley.com/doi/abs/10.1029/2010JD015139.

Ovalle, Alonso de. 1703. *An Historical Relation of the Kingdom of Chile*. A. and J. Churchill.

Painting, D. J. 2003. “AMDAR Reference Manual.” *World Meteorological Organization Tech. Rep. WMO* 958: 84.

Pessi, Antti T., and Steven Businger. 2009. “The Impact of Lightning Data Assimilation on a Winter Storm Simulation over the North Pacific Ocean.” *Monthly Weather Review* 137 (10): 3177–95.

Peyraud, Lionel. 2013. “Analysis of the 18 July 2005 Tornadic Supercell over the Lake Geneva Region.” *Weather and Forecasting* 28 (6): 1524–51.

Rasmussen, Erik A., and John Turner. 2003. *Polar Lows: Mesoscale Weather Systems in the Polar Regions*. Cambridge University Press.

Rasmussen, Erik N. 2003. “Refined Supercell and Tornado Forecast Parameters.” *Weather and Forecasting* 18 (3): 530–35.

Rasmussen, Erik N., and David O. Blanchard. 1998. “A Baseline Climatology of Sounding-Derived Supercell and Tornado Forecast Parameters.” *Weather and Forecasting* 13 (4): 1148–64.

Reed, Richard J., and Warren Blier. 1986. “A Further Study of Comma Cloud Development in the Eastern Pacific.” *Monthly Weather Review* 114 (9): 1696–1708.

Rose, Stanley F., Peter V. Hobbs, John D. Locatelli, and Mark T. Stoelinga. 2004. “A 10-Yr Climatology Relating the Locations of Reported Tornadoes to the Quadrants of Upper-Level Jet Streaks.” *Weather and Forecasting* 19 (2): 301–9.

Accepted for publication in *Bulletin of the American Meteorological Society*. DOI 10.1175/BAMS-D-19-0218.1.

Servicio Meteorologico de la Armada, Chile. 2010. “Evidencias de Fenómenos Del Tipo Tornado En Las Costas de La VIII Región Del Biobío Y El Sur de Chile.” Servicio Meteorologico de la Armada de Chile. http://meteoarmada.directemar.cl/prontus_meteo/site/artic/20101214/pags/20101214135557.html.

Sherburn, Keith D., and Matthew D. Parker. 2014. “Climatology and Ingredients of Significant Severe Convection in High-Shear, Low-CAPE Environments.” *Weather and Forecasting* 29 (4): 854–77.

———. 2019. “The Development of Severe Vortices within Simulated High-Shear, Low-CAPE Convection.” *Monthly Weather Review*. https://doi.org/10.1175/mwr-d-18-0246.1.

Sherburn, Keith D., Matthew D. Parker, Jessica R. King, and Gary M. Lackmann. 2016. “Composite Environments of Severe and Nonsevere High-Shear, Low-CAPE Convective Events.” *Weather and Forecasting* 31 (6): 1899–1927.

Silva Dias, Maria A. F. 2011. “An Increase in the Number of Tornado Reports in Brazil.” *Weather, Climate, and Society* 3 (3): 209–17.

Skamarock, William C., Joseph B. Klemp, Jimy Dudhia, David O. Gill, Zhiquan Liu, Judith Berner, Wei Wang, et al. 2019. “A Description of the Advanced Research WRF Model Version 4.” UCAR/NCAR. https://doi.org/10.5065/1DFH-6P97.

Soliño, A., and M. A. Schwarzkopf. 1982. “Ocurrencia de Tornados Sobre El Sector Sur Del Continente Americano.” In *Segundo Congresso Brasileiro de Meteorologia, Anais, Pelotas*.

Taszarek, Mateusz, Harold E. Brooks, Bartosz Czernecki, Piotr Szuster, and Krzysztof Fortuniak. 2018. “Climatological Aspects of Convective Parameters over Europe: A Comparison of ERA-Interim and Sounding Data.” *Journal of Climate* 31 (11): 4281–

Accepted for publication in *Bulletin of the American Meteorological Society*. DOI 10.1175/BAMS-D-19-0218.1.

4308.

Thompson, Gregory, Paul R. Field, Roy M. Rasmussen, and William D. Hall. 2008. “Explicit Forecasts of Winter Precipitation Using an Improved Bulk Microphysics Scheme. Part II: Implementation of a New Snow Parameterization.” *Monthly Weather Review* 136 (12): 5095–5115.

Thompson, Richard L., Corey M. Mead, and Roger Edwards. 2007. “Effective Storm-Relative Helicity and Bulk Shear in Supercell Thunderstorm Environments.” *Weather and Forecasting* 22 (1): 102–15.

Tsonevsky, Ivan, Charles A. Doswell, and Harold E. Brooks. 2018. “Early Warnings of Severe Convection Using the ECMWF Extreme Forecast Index.” *Weather and Forecasting* 33 (3): 857–71.

Turman, B. N., and R. J. Tettelbach. 1980. “Synoptic-Scale Satellite Lightning Observations in Conjunction with Tornadoes.” *Monthly Weather Review* 108 (11): 1878–82.

Vicencio, J., A. Reyes, Sánchez S., R. Padilla, J. Crespo, and D. Campos. 2019. “Informe Especial: Tornados En La Región Del Biobío.” Dirección Meteorológica de Chile. http://archivos.meteochile.gob.cl/portaldmc/meteochile/documentos/DMC-InfoEspecial_TornadosBiobio_v5black.pdf.

Virts, Katrina S., John M. Wallace, Michael L. Hutchins, and Robert H. Holzworth. 2013. “Highlights of a New Ground-Based, Hourly Global Lightning Climatology.” *Bulletin of the American Meteorological Society* 94 (9): 1381–91.

Wesolek, Emmanuel, and Pierre Mahieu. 2011. “The F4 Tornado of August 3, 2008, in Northern France: Case Study of a Tornadic Storm in a Low CAPE Environment.” *Atmospheric Research* 100 (4): 649–56.

Zipser, E. J., Daniel J. Cecil, Chuntao Liu, Stephen W. Nesbitt, and David P. Yorty. 2006. “WHERE ARE THE MOST INTENSE THUNDERSTORMS ON EARTH?” *Bulletin of*

Accepted for publication in *Bulletin of the American Meteorological Society*. DOI 10.1175/BAMS-D-19-0218.1.

the American Meteorological Society 87 (8): 1057–72.

Accepted for publication in *Bulletin of the American Meteorological Society.* DOI 10.1175/BAMS-D-19-0218.1.

TABLES

Table. 1. Main features of all tornadoes reported between May 30 and 31 of 2019, including informed location, hour, estimated intensity, path, and main observed damage. Report source: ONEMI (National Emergency Management Office), newspapers, DMC technical report, and social network.

#	**Location (City/Town , Region)**	**Lat. and Long.**	**Hour UTC** **DD/MM**	**Duration,** **Path distance,** **EF Scale (Estimated maximum winds)**	**Supercellular Features** **(total life, storm direction and speed, IR features)**	**Main observed damage according to different evidence and reports**
1	San Carlos/ Quilelto, Ñuble	-36.503º -71.973º	~ 19:00 30/05		2 h 20 min, 330º, 10 m s-1	- Roof damage and falling tree branches.
2	San Miguel de Itata, Yungay, Biobío	-37.106º -72.119º	~ 19:20 30/05		(17:20-20:30) 3h 10 min, 318º, 10 m s-1 -enhanced V	- Roof damage, broken glass and lamp posts destroyed. - 28 houses with minor damage, 14 houses with roof damage
3	Coihueco Ñuble	-36.726º -71.810º	~ 20:00 30/05		2 h 20 min, 330º, 10 m s-1 (same storm as tornado #1) -enhanced- V -coldest temperature updraft before tornado	- Roof damage, falling tree branches, and lamp posts destroyed. - Complete destruction of a wooden public dining room.
4	Los Ángeles, Biobío	-37.463° -72.330°	21:57 30/05	~ 8 min, ~ 5.0 Km, EF-2 (60.3 m s-1)	(20:00-22:40) 2 h 40 min, 328º, 12m s-1 -flanking line updrafts -coldest temperature updraft before tornado	- 18 people injured. - 345 people affected. - 11 houses destroyed, 119 with major damage and 213 houses with minor damage. - 1 wooden building completely destroyed. - Truck and cars displaced. - Fallen trees. - Roads blocked and

Accepted for publication in *Bulletin of the American Meteorological Society.* DOI 10.1175/BAMS-D-19-0218.1.

						affected. - 200 people without communication services. - 6.769 electricity customers affected by power outages.
5	Collipulli, Araucanía	-37.939° -72.438°	22:00 - 23.25 30/05		(21:20-23:10) 1 h 50 min, 328ª, 12 m s-1	- 13 people injured. - 17 people affected. - 1 house destroyed, 1 house with major damage and 4 other houses with minor damage.
6	Talcahuano / Concepción , Biobío	-36.785° -73.100°	18:00 31/05	15 min 17.1 km EF-1 (42.2 m s-1)	(15:40-18:30) 2h 50min, 329º, 18 m s-1 -cold U	- 1 person dead. - 23 people injured. - 1 house destroyed, 175 with major damage and 191 with minor damage. - Near 500 houses with different types of damage. - Around 50,000 electricity customers affected by power outages.
7	Chanco, Maule	-35.775° -72.505°	Between 19:00 and 19:20 31/05		(17:40-19:40) 2h, 318º, 22 m s-1 -cold U	- Fallen trees and power outages in rural areas. - Roads blocked.
(*) ONEMI: Oficina Nacional de Emergencias (National Emergency Management Office).						

834

Accepted for publication in *Bulletin of the American Meteorological Society.* DOI 10.1175/BAMS-D-19-0218.1.

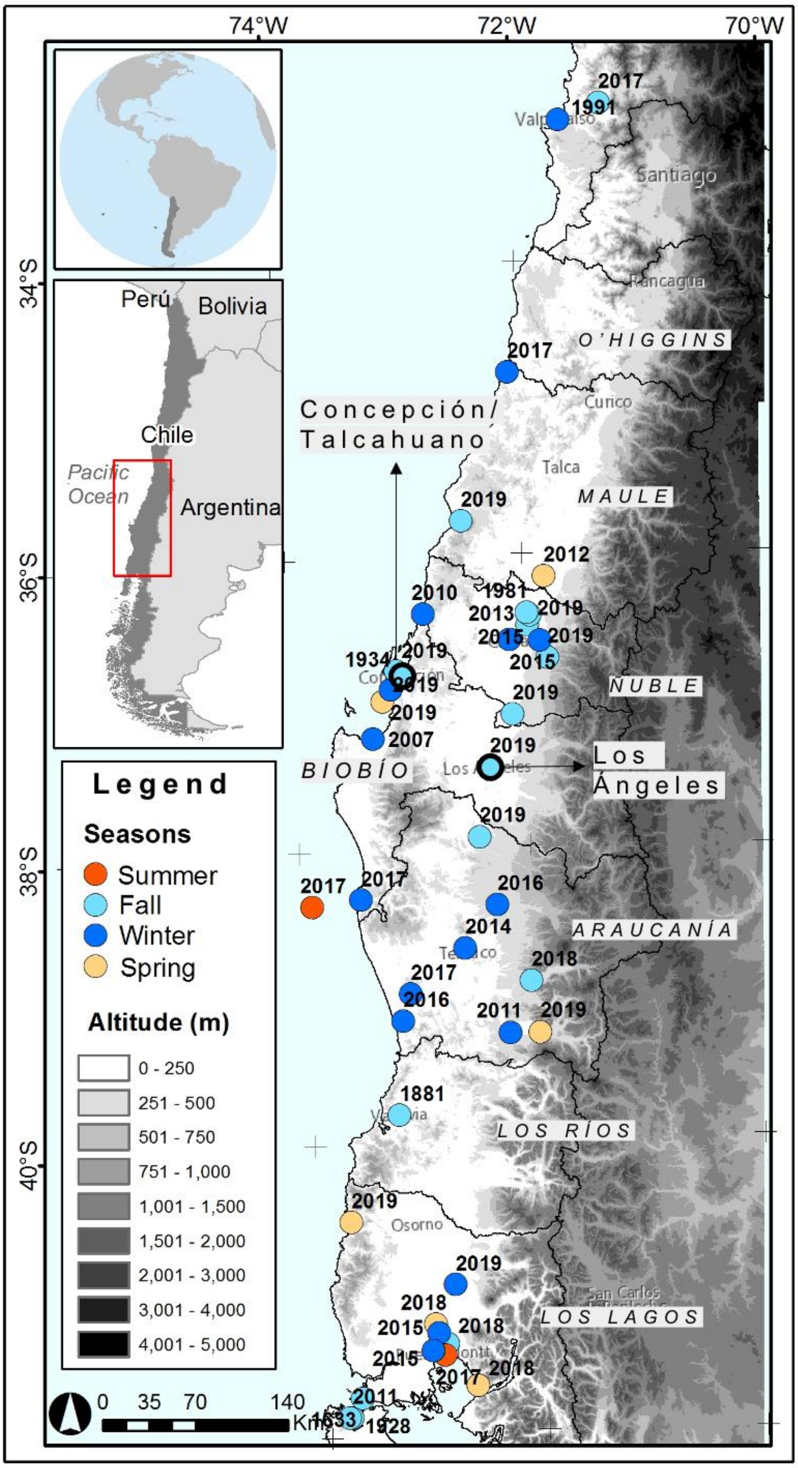

Fig. 1. Geographical location of Central and Southern Chile, including the position of 37 reported tornadoes (filled circles) from 1633 to 2019, including season (color) and year of occurrence, according to Servicio Meteorologico de la Armada (2010) and own elaboration. Positions of Talcahuano-Concepción and Los Ángeles are shown in the black contour circle. Topography is shown in grayscale. Administrative region's name is indicated in black cursive font.

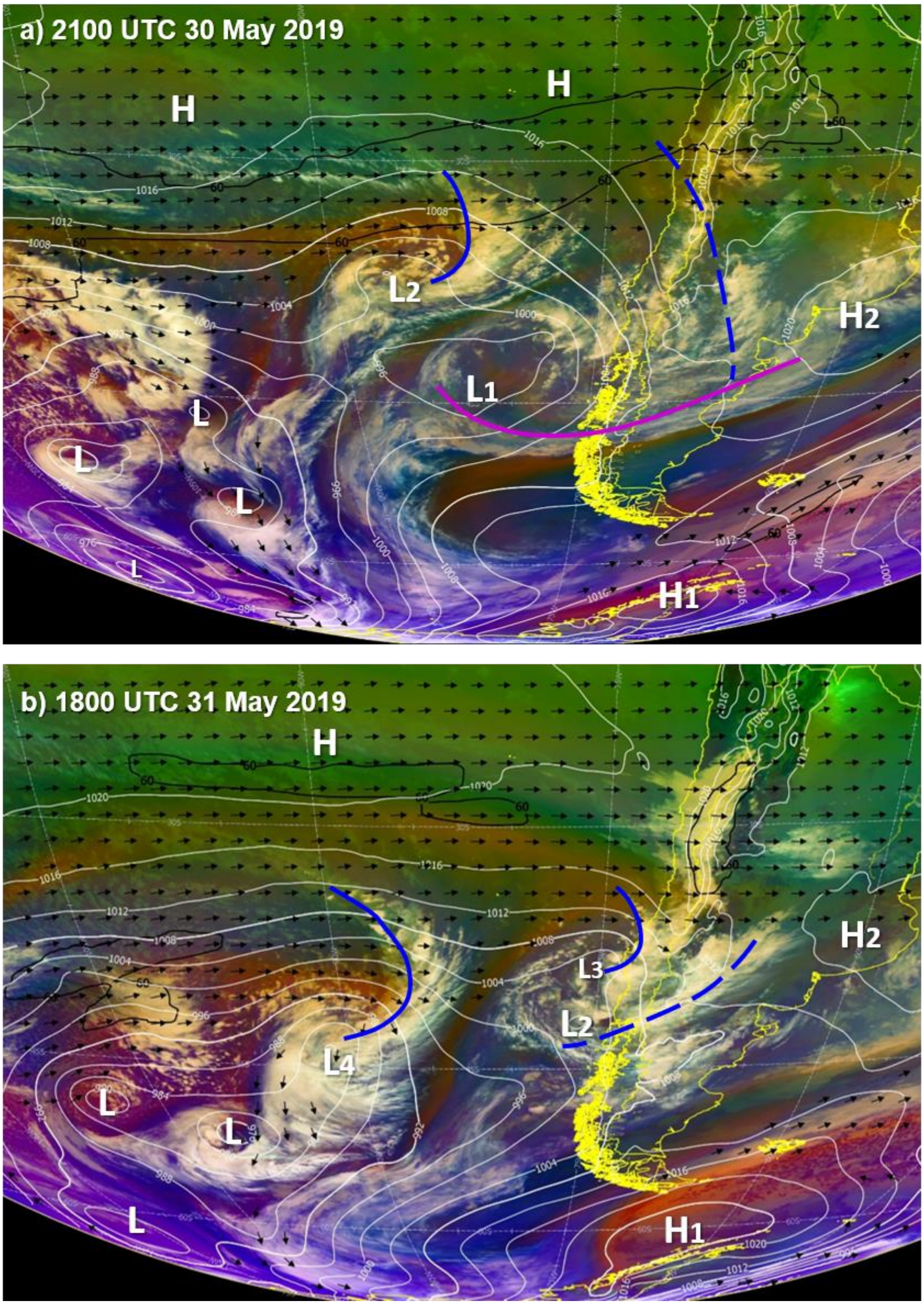

Fig. 2. Airmass-RGB composite from GOES-16 (colors), sea-level pressure every 2 hPa (white lines), winds at 300 hPa > 40 m s^{-1} (black arrows), and > 60 m s^{-1} (black contours) for (a) 2100 UTC 30 May 2019 and (b) 1800 UTC 31 May 2019 (b). Cold and occluded front symbols (blue and magenta lines, respectively) and approximate location of high (H) and low (L) pressure centers are included. Important pressure centers are numbered (see in text). Synoptic data obtained from ECMWF (0.1°x0.1°).

Accepted for publication in *Bulletin of the American Meteorological Society.* DOI 10.1175/BAMS-D-19-0218.1.

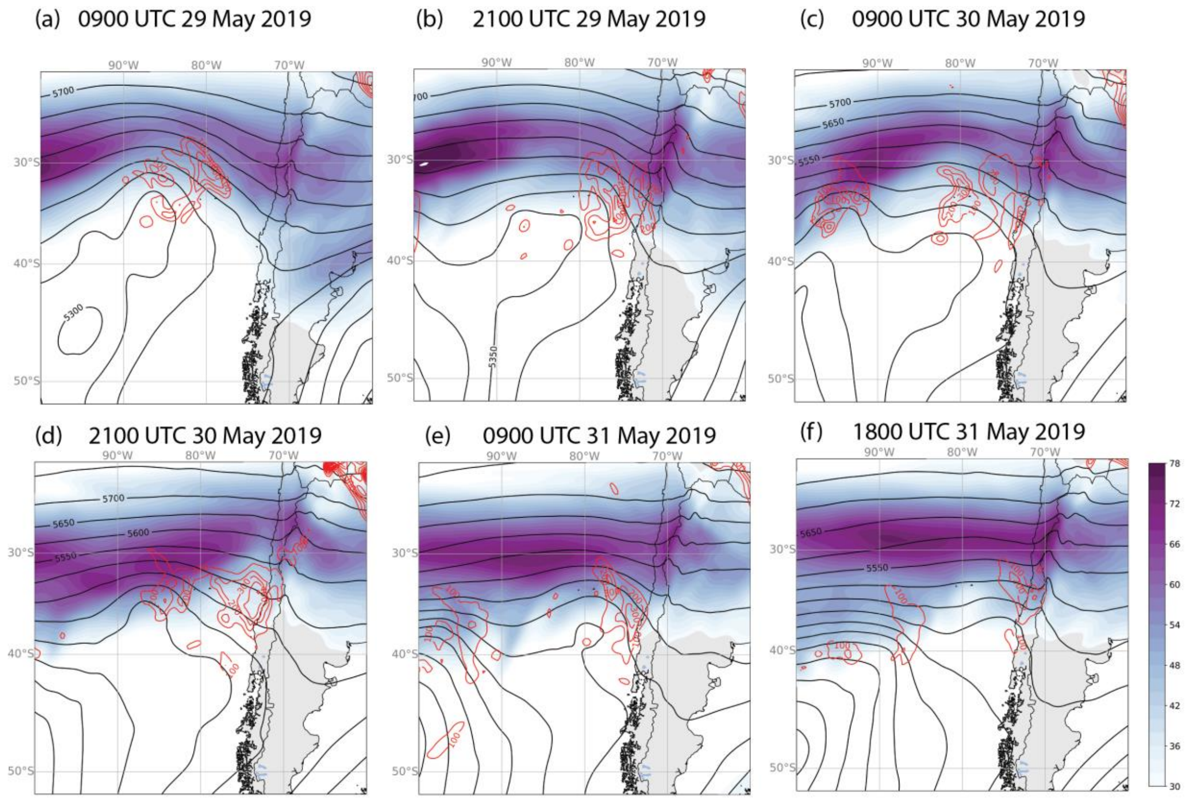

Fig. 3. Wind at 200 hPa (colors, m s-1), Geopotential height at 500 hPa (black contours, m), most unstable CAPE (J/kg) (red contours). Atmospheric fields are from the ERA-5 reanalysis.

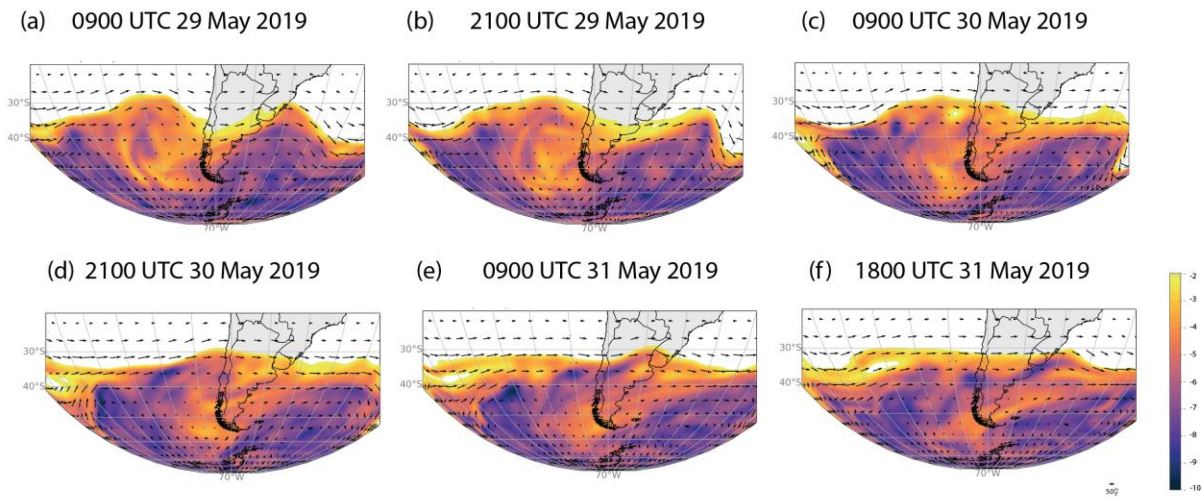

Fig. 4 Potential vorticity at 330 K isentropic surface (color, PV units) and wind at 330 K isentropic surface. Atmospheric fields are from ERA-Interim reanalysis.

Accepted for publication in *Bulletin of the American Meteorological Society.* DOI 10.1175/BAMS-D-19-0218.1.

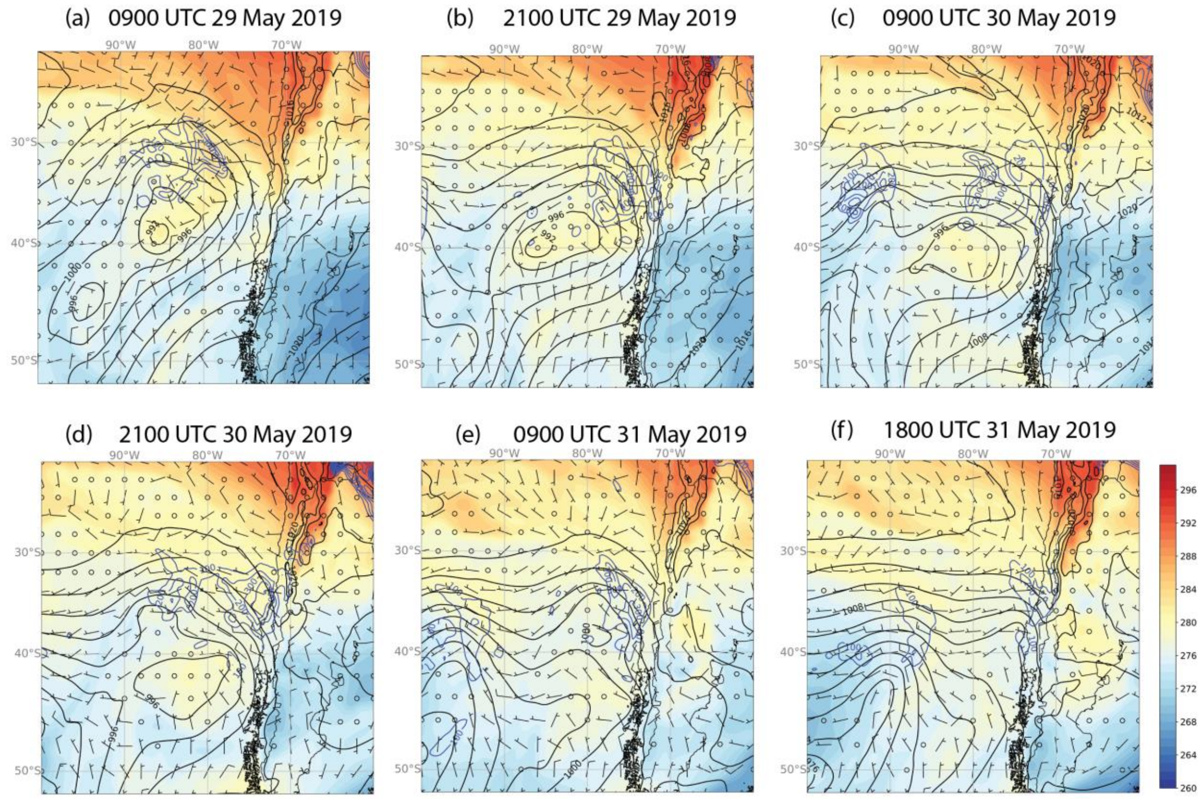

Fig. 5. Mean sea level pressure (hPa, black contours), wind shear between 850 hPa and surface (barbs, m/s), temperature at 850 hPa, (K) (colors), most unstable CAPE (J/kg) (blue contours) for (a) 0900 UTC 29 May 2019, (b) 2100 UTC 29 May 2019, (c) 0900 UTC 30 May 2019, (d) 2100 UTC 30 May 2019, (e) 0900 UTC 31 May 2019, and (f) 1800 UTC 31 May 2019. Atmospheric fields are from the ERA-5 reanalysis.

Accepted for publication in *Bulletin of the American Meteorological Society.* DOI10.1175/BAMS-D-19-0218.1.

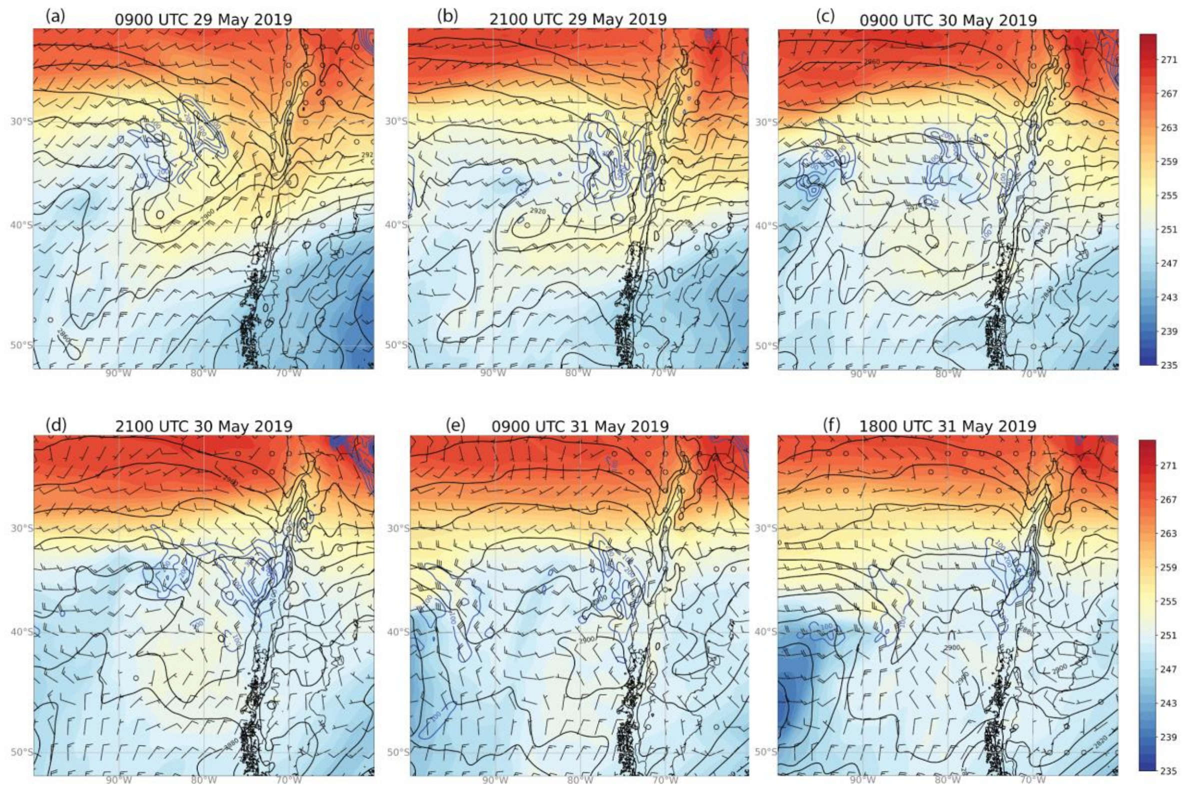

Fig. 6. Wind at 850 hPa (barbs in m s-1), thickness between 1000 and 700 hPa (black contours, m), temperature at 500 hPa (color-shaded, K), and most unstable CAPE (blue contours, J kg^{-1}), for (a) 0900 UTC 29 May 2019, (b) 2100 UTC 29 May 2019, (c) 0900 UTC 30 May 2019, and (d) 2100 UTC 30 May 2019 (e) 0900 UTC 31 May 2019 (f) 1800 UTC 31 May 2019. Atmospheric fields are from the ERA-5 reanalysis.

Accepted for publication in *Bulletin of the American Meteorological Society.* DOI 10.1175/BAMS-D-19-0218.1.

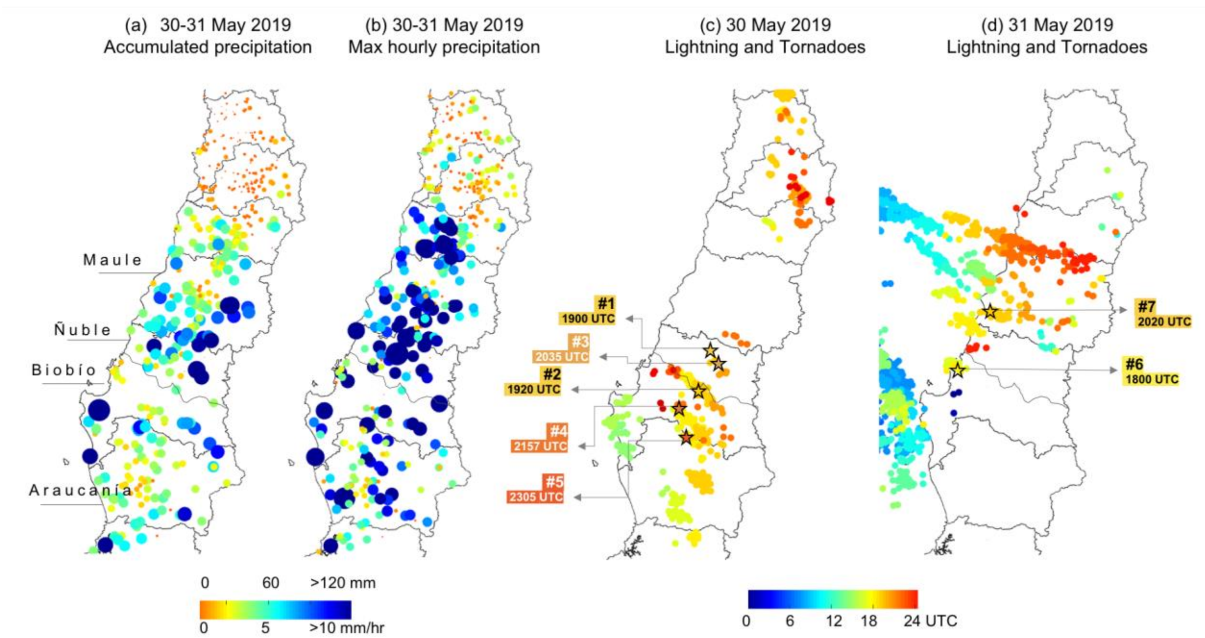

Fig. 7. In panel (a), total accumulated precipitation during 31 and 31 May 2019 (mm); in panel (b), maximum hourly precipitation (mm/hr) observed during 30 and/or 31 May 2019; in (c) and (d), lightning (colors) and tornado report (black star) during 30 May (c) and 31 May 2019 (d). Tornado order (#1 to #7) is also indicated according to the hour of occurrence (see Table 1).

Accepted for publication in *Bulletin of the American Meteorological Society.* DOI 10.1175/BAMS-D-19-0218.1.

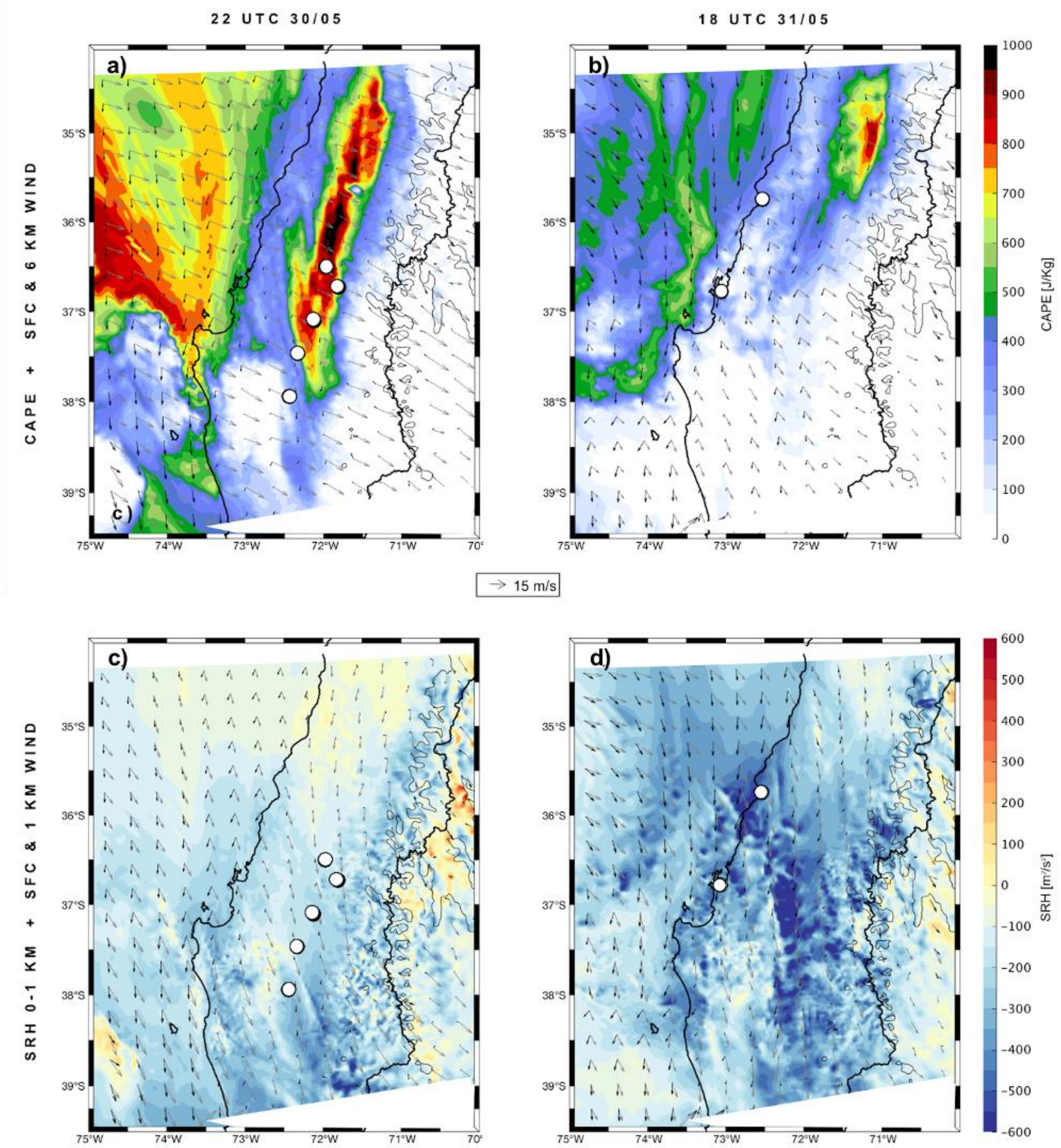

Fig. 8. In the upper panels, the most unstable CAPE (shaded colors), surface wind (black arrows), and 6 km winds (gray arrows). In the bottom panels, storm-relative helicity (SRH) 0-1 km (shaded colors), surface wind (black arrows), and 1 km winds (gray arrows). Left panels correspond to 2200 UTC 30 May and right panels to 1800 UTC 31 May 2019. Tornado locations are plotted in white circles. The Andes Cordillera area is plotted in thin black contours (>3 km height above sea level). Data from WRF simulations using 1-km horizontal resolution domain.

Accepted for publication in *Bulletin of the American Meteorological Society.* DOI 10.1175/BAMS-D-19-0218.1.

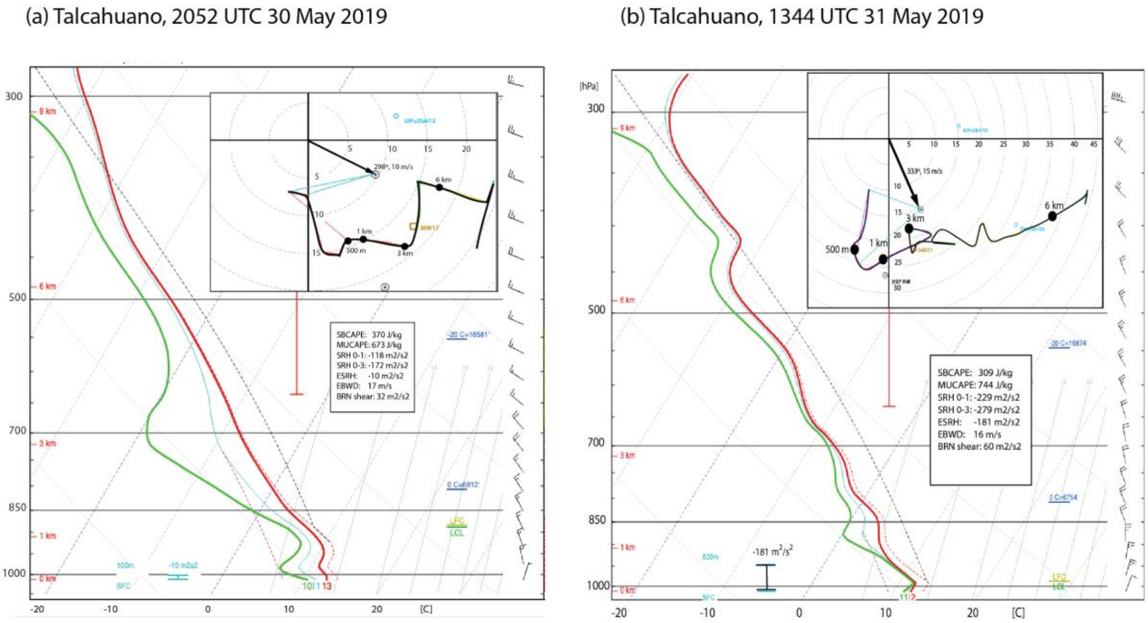

Fig. 9. Skew-T log-P diagrams and hodographs for the AMDAR profiles of (a) 2052 UTC 30 May 2019 and (b) 1344 UTC 31 May 2019 at Talcahuano, adapted from SHARPpy (Blumberg et al. 2017). Red line is the temperature profile, and the green line is the dew point (humidity is taken from WRF to construct these profiles). The hodographs show the storm motion for the left-mover storm (arrows, Bunkers et al. 2014). 500m, 1 km, 3 km, and 6 km AGL are marked by black dots in the hodograph. The insets show the values of several typical supercell parameters, as calculated by SHARPpy for each sounding.

Accepted for publication in *Bulletin of the American Meteorological Society*. DOI 10.1175/BAMS-D-19-0218.1.

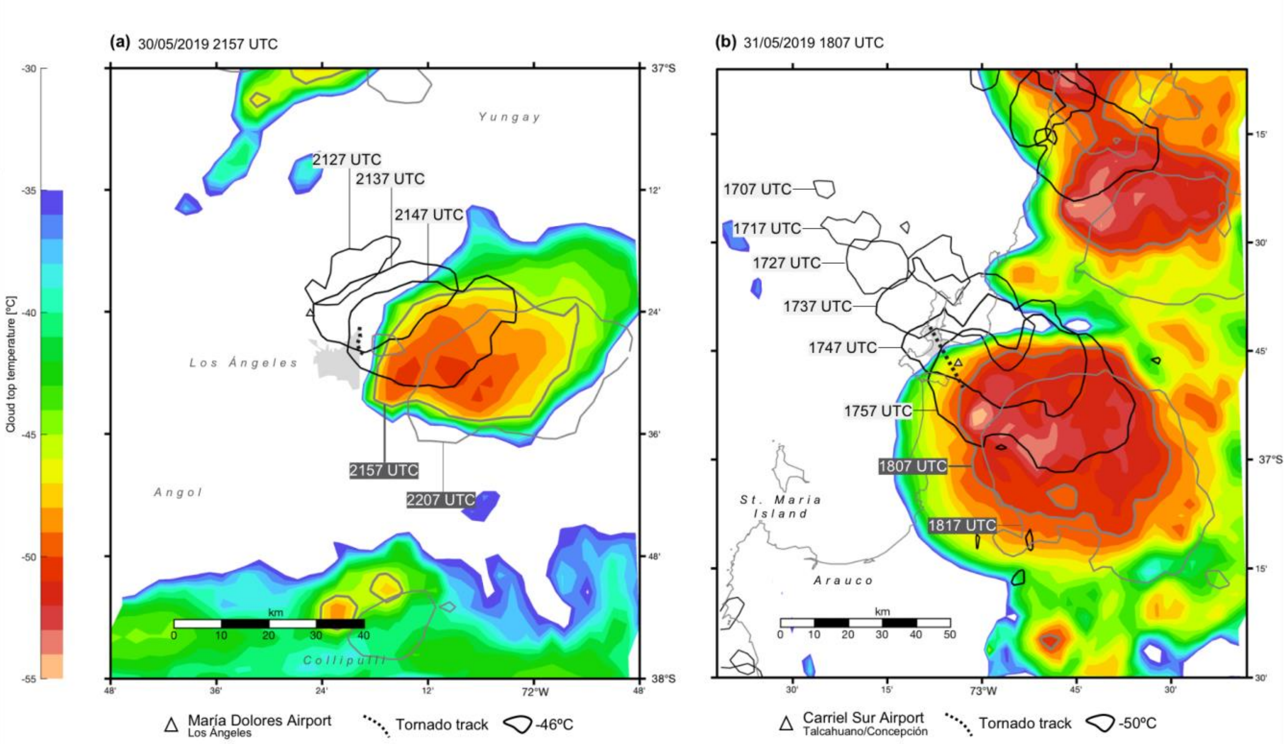

Fig. 10. Cloud-top temperature from infrared satellite image (channel 13, GOES-16, ºC in color-shaded) at tornado moment: 2157 UTC 30 May for Los Ángeles (a) and 1807 UTC 31 May for Talcahuano-Concepción (b). We also plotted the storm evolution considering the cloud-top temperatures of -46ºC (a) and -50ºC (b) every ten minutes before the appearance of the tornadic storm, in black contours, and after the tornado, in gray contours. Dashed black line corresponds to tornado path at surface. Light gray areas represent urban zones, corresponding to Los Ángeles (a) and Talcahuano-Concepción (b). Triangles can also help to reference the cities' positions: in (a) María Dolores Airport of Los Ángeles and (b) Carriel Sur Airport of Talcahuano. Data were obtained from GOES-16/17 on Amazon Download Page, Department of Atmospheric Science, University of Utah.

Accepted for publication in *Bulletin of the American Meteorological Society*. DOI 10.1175/BAMS-D-19-0218.1.

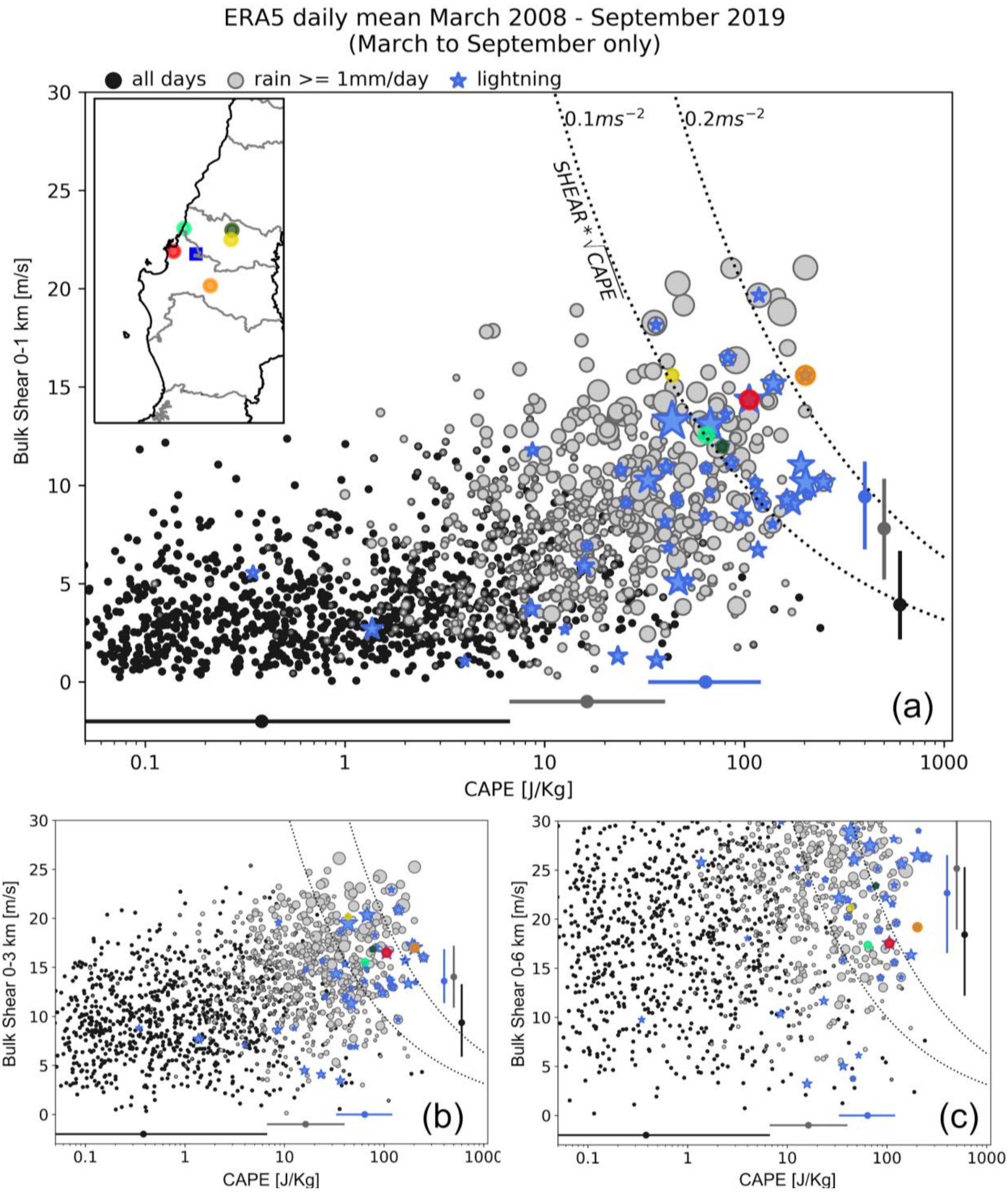

Fig. 11. Instability-shear joint distribution over the Biobío region. Each symbol represents one day during fall-winter (March–September) from 2008 to 2019. The horizontal axis is the daily mean most unstable CAPE (note the logarithmic scale), and the vertical axis is the daily mean magnitude of the wind shear in a column centered at 37°S, 72°W (blue square in inset, halfway between Concepción and Los Ángeles) between surface and (a) 1 km AGL, (b) 3 km AGL, and (c) 6 km AGL. Daily means are computed from hourly ERA-5 data. Black circles are dry days, gray circles are rainy days (>1 mm in the central box) with their size proportional to daily accumulation (the larger circles are about 70 mm/day), and blue stars are days with more than

Accepted for publication in *Bulletin of the American Meteorological Society*. DOI 10.1175/BAMS-D-19-0218.1.

25 WWLLN lightning strokes in a 3°´3° box centered at 37°S, 72.5°W, with their size proportional to daily number. Black, gray, and blue lateral bars (dots) indicate the interquartile range (median) of CAPE/shear during dry, rainy, and lightning days, respectively. The conditions on 30 and 31 May 2019 are identified by the orange and red circles, respectively. Dotted lines indicate lines of constant 0–1-km shear times square root of CAPE in units of m s^{-2} ($VGP_{0\text{-}1}$).

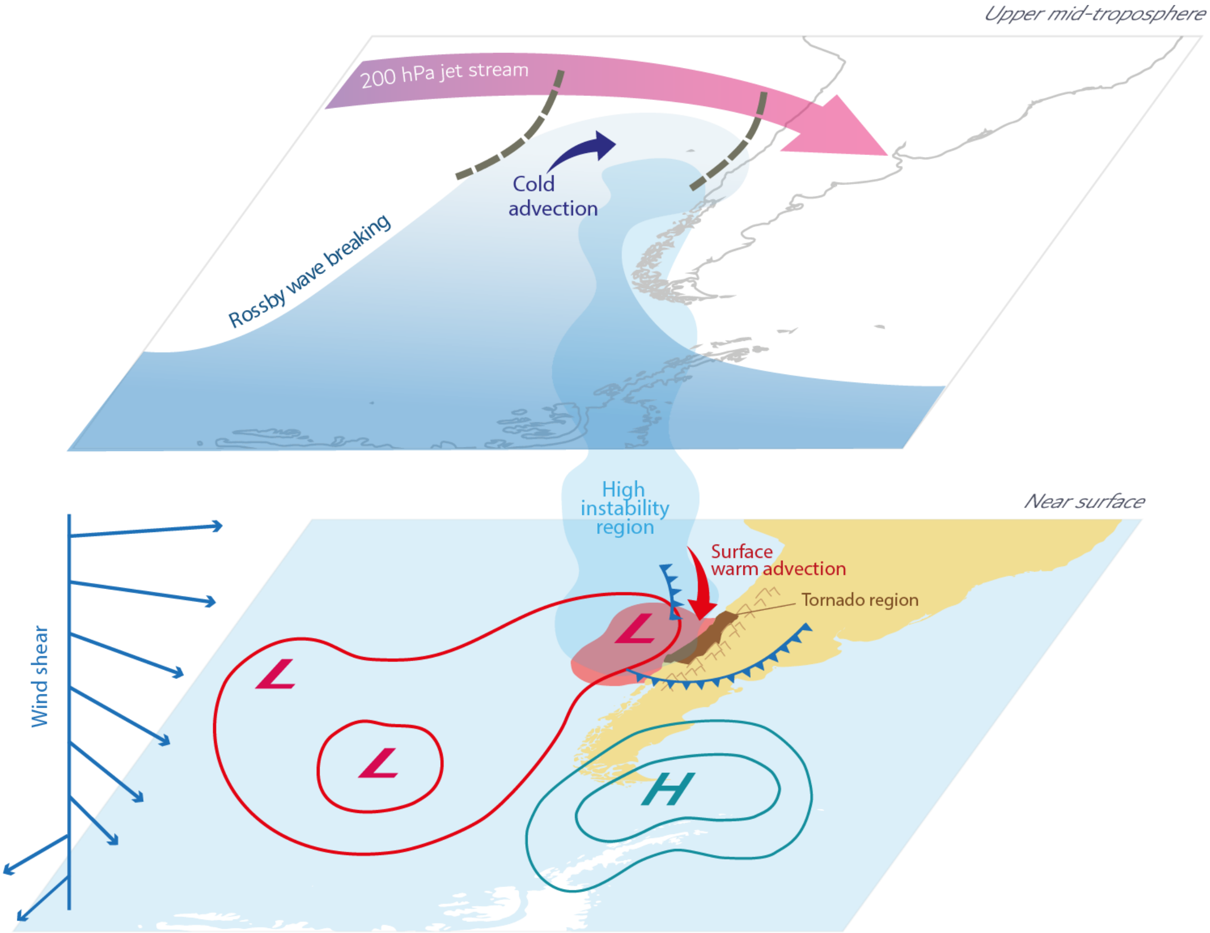

Fig. 12. Conceptual model summarizing synoptic main features of tornadic storms during the May 2019 outbreak. Top panel: dynamical features of the upper and mid-troposphere, highlighting the position of the jet stream, cold advection, shortwaves (dashed lines) and Rossby wave breaking. Bottom panel: dynamical features near the surface, highlighting the wind shear profile, surface warm advection, position of the blocking high (H) and low-pressure centers (L).

Accepted for publication in *Bulletin of the American Meteorological Society*. DOI 10.1175/BAMS-D-19-0218.1.

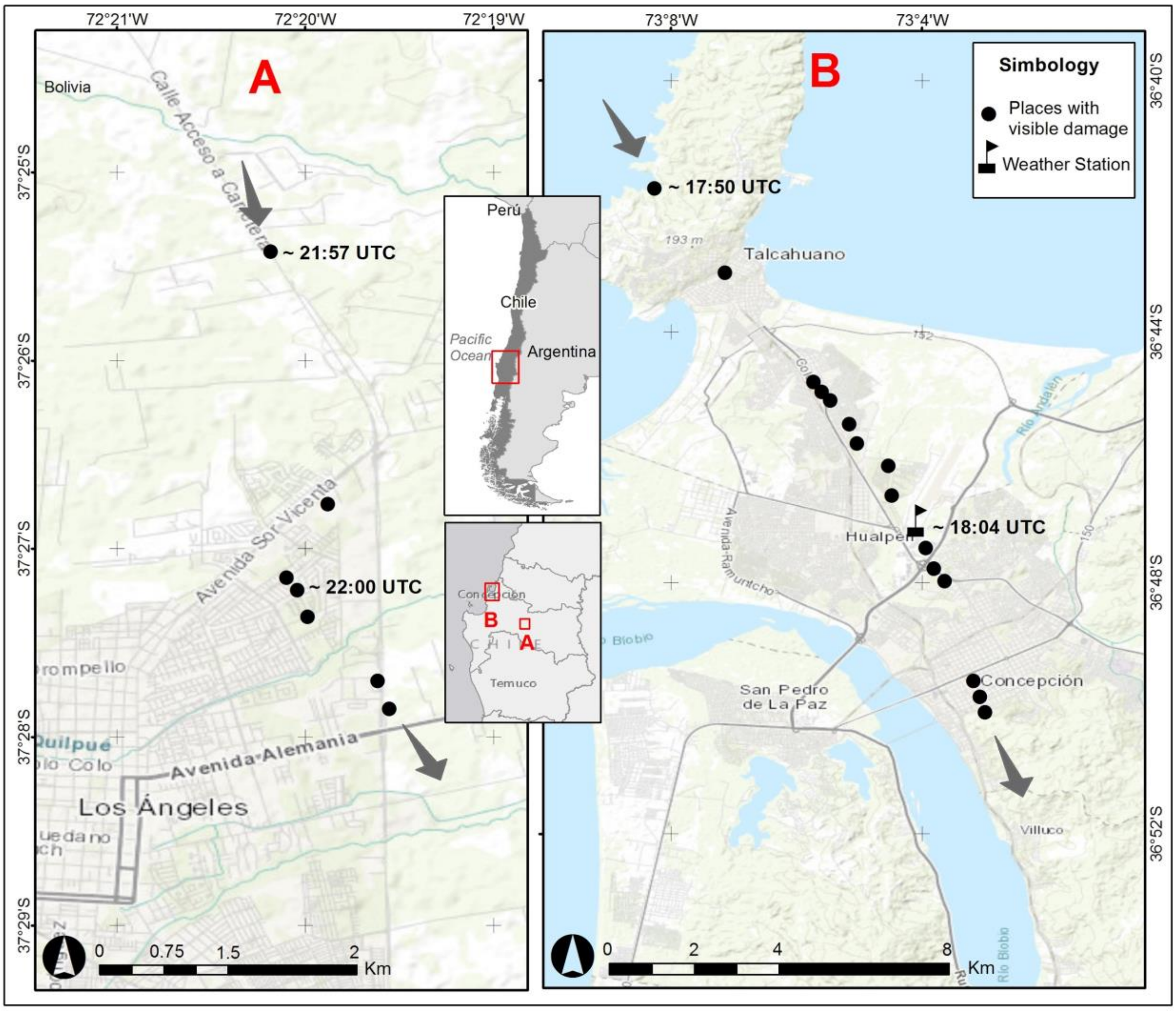

Fig. A1. Tornado trajectory and damage points reported in Los Ángeles (a) and Talcahuano-Concepción (b), including the location of known affectation hours in UTC. The flag symbol indicates the location of Carriel Sur Airport's weather station.

Accepted for publication in *Bulletin of the American Meteorological Society.* DOI 10.1175/BAMS-D-19-0218.1.

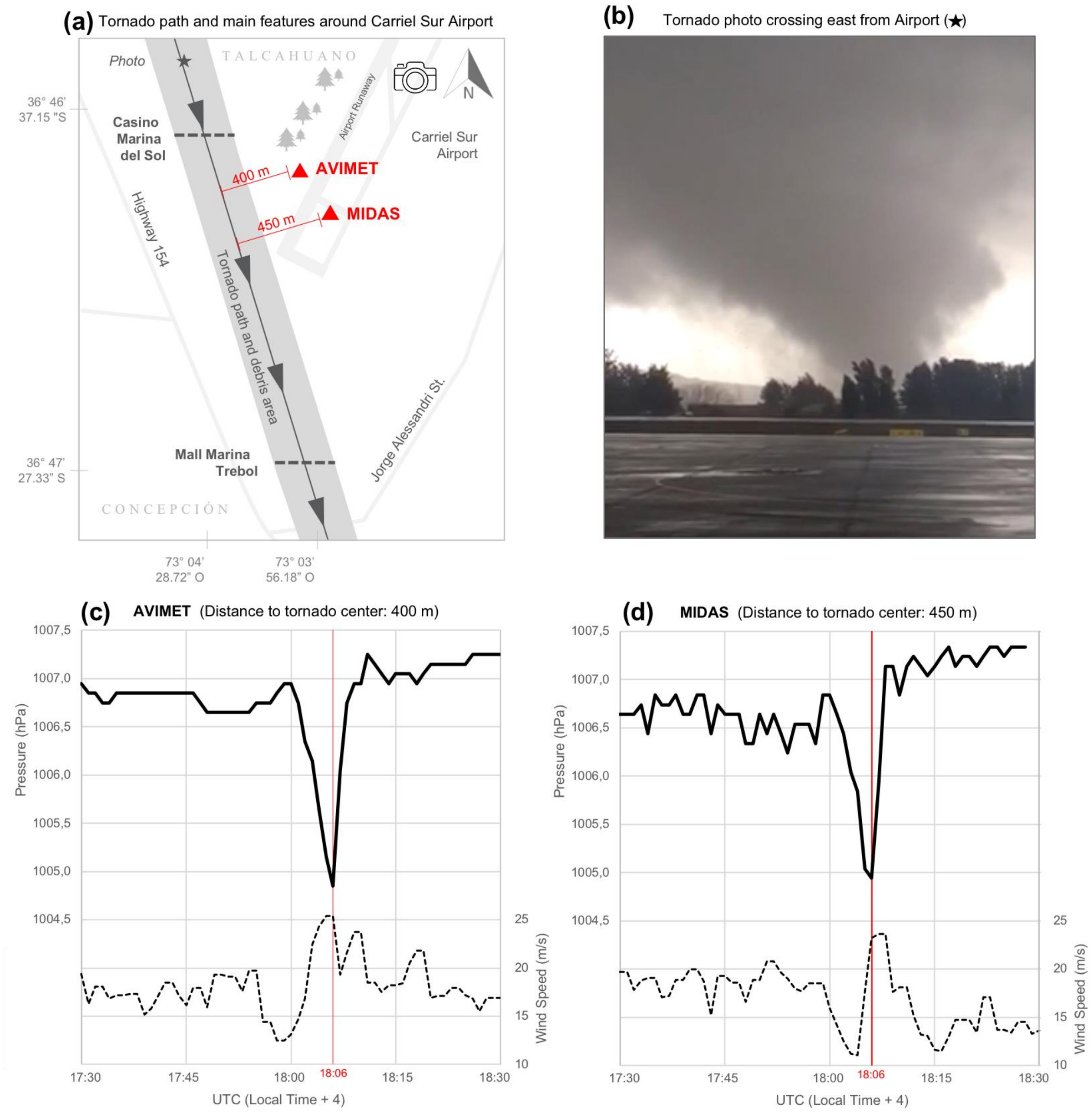

Fig. A2. In the upper-left panel, (a) tornado path (gray solid line), estimated width according to main debris area (shadow area), and principal features around Carriel Sur Airport, located between Talcahuano and Concepción; including two buildings with major damage (horizontal dashed line) and the location of two weather stations (red triangles). In the upper-right panel (b), a photograph of the tornado passing east from Carriel Sur after Casino Marina del Sol (taken by Airport-DGAC personnel from the landing track. Camera symbol indicates the direction toward the star symbol in panel a). In bottom panels, AVIMET (c) and MIDAS (d) weather stations with measures of surface pressure (black solid line) and 10 m instantaneous wind speed (black dashed line), located 400 and 450 m from tornado center, respectively.

Accepted for publication in *Bulletin of the American Meteorological Society*. DOI 10.1175/BAMS-D-19-0218.1.